Parametric study of density down-ramp injection in laser wakefield acceleration

Henrik Ekerfelt

Lund University

Master of Science in Engineering,
Engineering Physics
Division of Atomic Physics
Degree Project in Physics
PHYM01 – 2014/2015

Supervisors:
Olle Lundh
Martin Hansson

Abstract

In laser wakefield acceleration (LWFA) a high intensity laser pulse is used to excite a plasma density wave with an associated electric field. This electric field can be used to accelerate electrons. However, to be accelerated the electrons first of all need to enter the plasma wave. This process is called injection. In this thesis a scheme for injecting electrons into a laser wakefield accelerator is studied. Focus lies on particle-in-cell simulations performed on a computer cluster. A parametric scan is performed where a density down-ramp's slope and length is varied. A linear relation between the density down-ramp length and injected charge is shown. Furthermore a small density difference is shown to yield higher electron energies. A logarithmic relation between the density down-ramp slope and injected charge is shown. The slope can be optimised to control the spatial distribution of injected electrons within the plasma wave. A high peak current is shown to preserve a mono-energetic distribution over the acceleration length.

A number of simulations is performed to explain experimental results where a large variation of injected charge is shown. A second injection mechanism is identified as the source of a large variation in injected charge.

An imaging diagnostic system with a resolution of 2 μm looking at the Thomson scattered light from the laser pulse is designed and implemented. The Thomson scattered light is proportional to the background density of the electrons, and could therefore be used to detect density gradients.

Acknowledgements

A lot of people have been involved in getting this project done. I would especially like to acknowledge the help from and thank:

My supervisor Olle Lundh for the idea, the help, and all the insightful conversations. My second supervisor Martin Hansson, for the support and guidance. My informal supervisor Xavier Davoine, who taught me how to use CALDER-CIRC, and always answered my questions patiently. Isabel Gallardo for the great collaboration and the support. Claes-Göran Wahlström, for inviting me to do my master thesis with the group and taking the time to answer my questions. The rest of the ultra high intensity group, Anders Persson, Kristoffer Svensson, and Lovisa Senje for all the help and discussions. Simon Segerblom Rex for all the help with LaTeX and great collaboration during our years together at the university.

Ellen Brydevall, for everything that matters.

'And you?' she said, turning to Sam. 'For this is what your folk would call magic, I believe; though I do not understand clearly what they mean; and they use the same word of the deceits of the Enemy. But this, if you will, is the magic of Galadriel. Did you not say that you wished to see Elf-magic?'

- J.R.R. Tolkien, The Lord of the Rings: The Fellowship of the Ring.

Contents

Abstract i

Acknowledgements ii

1 Introduction 1
- 1.1 Purpose . . . 3
- 1.2 Structure . . . 4

2 Laser Wakefield Acceleration 5
- 2.1 Plasmas . . . 5
- 2.2 Plasma frequency . . . 5
- 2.3 Electromagnetic waves in vacuum . . . 7
- 2.4 Electromagnetic waves in plasmas . . . 9
- 2.5 Pondermotive force . . . 10
- 2.6 Electron density waves driven by a laser pulse . . . 12
- 2.7 Injection and trapping . . . 14
  - Density down-ramp injection . . . 15

3 Numerical method 18
- 3.1 PIC-code . . . 18
- 3.2 CALDER-CIRC . . . 20
  - Fourier decomposition of the laser field . . . 21
  - Courant–Friedrichs–Lewy condition . . . 22
  - Scalability . . . 22
  - Normalisation . . . 23
- 3.3 Simulations . . . 23

4 Experimental method 24
- 4.1 Multi-Terawatt Laser system at Lund Laser Centre . . . 24
- 4.2 Experimental setup . . . 24
- 4.3 Top-view diagnostics . . . 26
  - Thomson scattered light . . . 26
  - Top-view . . . 27

5 Result and discussion **31**
5.1 Top-view 31
Results and discussion 31
5.2 Studies of density down-ramp injection 35
Results and discussion 35

6 Conclusion and Outlook **46**

References **48**

Appendices

A Multi-Terawatt Laser system at Lund Laser Centre **51**

B CALDER-CIRC input file **53**

C CALDER-CIRC outputs **57**
C.1 Diag spat 57
C.2 Diag phase 58

D Populärvetenskaplig artikel **59**

Chapter 1

Introduction

Highly energetic particles play an important role today. On the research frontier, 17 billion SEK is invested only in Lund to build high-energy particle facilities over the coming decade. Most of the money (14 billion SEK) goes into the European Spallation Source (ESS), the world's most powerful neutron source, to be used for neutron imaging. The rest goes to the Swedish national laboratory MAX IV, which will produce synchrotron radiation from electrons travelling in a storage ring. At the European organisation for nuclear research (known as CERN) outside Geneva, the mecca of fundamental particle physics, the Large Hadron Collider (LHC) is producing proton beams at energies never produced by humans before.

These multi-billion facilities do not only contribute to discovering new particles or mapping the complex proteins around us. The diagnostics put extreme demands on data processing, high performance diagnostics and structures that can withstand both mechanical stress and radiation. All this cutting-edge engineering work strongly influences our lives today. For example, the world wide web was born at CERN!

In health care, radiation therapy is a key component in the treatment of cancer. X-ray imaging is still widely used as a fast diagnostic. High-energy particles are also used to produce radioisotopes which can be tracked within living creatures.

In high-energy physics, the conventional accelerators used today are reaching their limits. To reach higher energies, enormous constructions would be needed. For example the LHC already require a tunnel with a circumference of 27 km! One limiting factor is the radio frequency (RF) cavities used to accelerate charged particles. They can only sustain an electric field of 50 MV/m before they break down due to ionisation of the cavity walls. Moreover, particles moving in a circular motion lose energy that scales with their momentum when bending the beam. These two factors together results in the fact that for higher energies, larger constructions will be needed.

In other applications particle accelerators still require large constructions, even though they're smaller than the LHC. This could be problematic, since

they, for example, might be hard to fit into a hospital. This therefore limits the energies that can be reached in such facilities. For example, one of the world's few Free Electron Lasers (FEL) at SLAC, Palo Alto, California, is fed with electrons accelerated over a few kilometers.

For the past 15 years or so, a novel particle accelerating scheme has been researched, where the acceleration takes place in a plasma. The scheme is based on the ability of a plasma to sustain large electric fields. This scheme is called laser wakefield acceleration (LWFA), see Figure (1.1). In LWFA, a laser pulse with a power on the TW scale is used. The pulse throws away all electrons from its path leaving an electron density perturbation with an associated electric field in its wake of the order of TV/m. This wakefield can be used to accelerate electrons to multi-GeV energies over cm distances as recently experimentally shown by Leemans et al. [1].

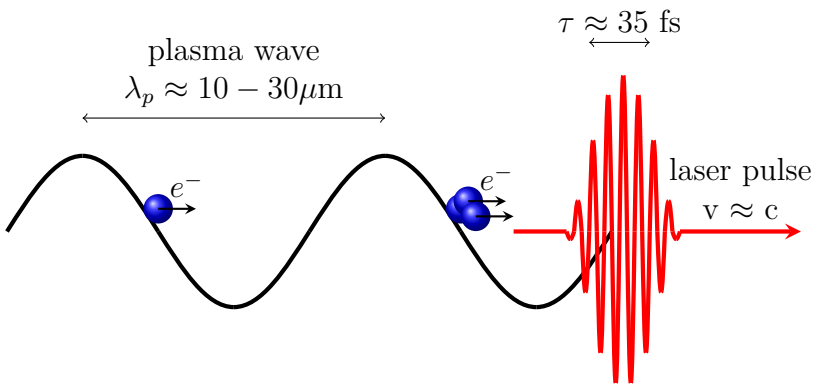

Figure 1.1: A schematic picture of Laser Wakefield Acceleration (LWFA). A short high intensity laser pulse drives a plasma density wave. In this plasma wave, electrons can be accelerated.

The idea was first proposed in 1979 by Tajima and Dawson in 1979 [2]. In the nineties the lasers had become strong enough to realise the idea experimentally. However, the bunches of electrons had large energy spreads and the number of electrons was decreasing with the energy.

In 2004, the research field had a major break-through when 3 groups [3, 4, 5] independently reported that quasi-monoenergetic bunches were accelerated in the so-called bubble regime.

The field has promising future applications, such as a table-top FEL, as a key component in radiation therapy or as an injector of electrons into larger particle accelerators, to name a few. Lasers are developing fast, and high-power lasers shrink in size, more importantly, they do not need to be in a linear construction, but the laser beams can easily be guided with mirrors.

However, there are still big issues remaining to get LWFA to work. It has been a hot research topic for 15 years. Produced beam energies are more than high enough to use in applications, but something is missing. In order to be useful for applications, wakefield accelerators have to produce the same characteristic electron bunch for every shot, in other words, they need to be reproducible. Part of the problem lies in controlling the acceleration length, a difference of a few hundred micrometers can change the energy of the electrons significantly. The uncertainty in acceleration length stems from where the acceleration starts rather than where it ends. The process when electrons starts to be accelerated is called electron injection or trapping, where a small amount of the oscillating background electrons enters the wakefield behind the laser pulse and starts their accelerating journey. Today focus lies on target engineering to achieve control of the injection mechanism. There are several ways to do this, further explained in Chapter 2.

1.1 Purpose

The work is performed in close connection with the ongoing work of the ultra high intensity laser physics group at the division of Atomic Physics at Lund University.

The physics in LWFA happens on sub-picosecond time scales. Our ability to monitor the processes is limited, and research groups around the world rely to a large extent on numerical simulations to understand the underlying physical processes. There are different schemes to simulate plasmas, one of the most common ways is through particle-in-cell (PIC) codes. Up until now, there has been no in-house capacity to run plasma simulations. An underlying goal of this project is for the group to learn and gain experience from PIC-simulations.

A better understanding of the injection and trapping mechanism is needed. Experiments from research groups show that density modulating injection schemes can be used to produce stable, controllable, high-quality bunches of accelerated electrons [6, 7]. The overall purpose of this thesis is to study the physics of a mechanism for injection called density down-ramp injection through simulations.

In addition, an easy way to experimentally detect density changes in the plasma channel formed by the laser pulse would be beneficial. An optical diagnostic to image light from the laser pulse, scattered by the plasma, is simple in its nature, easy to set up and does not take focus from the ongoing experiments. A second purpose of this thesis is to design, set up, test and evaluate such an imaging system with high resolution.

1.2 Structure

This thesis is divided into six chapters. Chapter 2 introduces the reader to the field of wake field acceleration. Chapter 3 introduces PIC-codes used to simulate the Laser Wakefield Acceleration process. The simulation code used for this thesis, CALDER-CIRC, is also described here. The last part of this chapter describes and motivates the simulation scenarios performed. The experimental setup is described in Chapter 4, from the laser to the electron detector. It also covers the imaging system looking at Thomson scattered light in more detail. The results from this thesis project is presented and discussed in Chapter 5. Finally the work is summed up in Chapter 6.

The thesis contains three appendices. In Appendix A the Multi-Terawatt Laser system at Lund Laser Center is described. In Appendix B a CALDER-CIRC input file is described. In Appendix C typical CALDER-CIRC output files are described. Appendix D contains a popular science article in Swedish.

Chapter 2

Laser Wakefield Acceleration

The fundamentals of the physics of laser wakefield acceleration (LWFA) are introduced in this chapter. General properties of plasma and laser physics are first discussed. Combining these, LWFA is then introduced. In the last part of this chapter, mechanisms for injection and trapping of electrons are discussed, which is the main focus of this thesis.

2.1 Plasmas

This section introduces the plasma as a state of matter. There are four states of matter: solid, liquid, gas and plasma. The most uncommon of these on Earth is plasma. However, almost everything in the observable universe consists of this fourth state of matter.

A plasma consists of charged particles. For example, a gas that is hot enough for the electrons to leave their respective nucleus is a plasma. A characteristic property of plasmas is the interaction between particles over distance. In a gas or liquid, atoms and molecules are typically electrically neutral and interact with each other mainly through collisions at small distances. The interaction in solids can be described by models where a vibrating atom will transfer energy to its nearest neighbours. However, in a plasma, since the particles are charged, they will interact over longer distances through electromagnetic interaction in addition to collisions. This gives rise to physics unseen in the other three states.

In this thesis only quasi-neutral plasmas are encountered, where the sum of all charge in the plasma is zero.

2.2 Plasma frequency

One of the more fundamental properties of a plasma is its oscillation frequency, ω_p, derived here. The oscillation frequency is important to be able to understand the plasma wave created behind the laser pulse.

A neutral plasma with locally displaced charge will give rise to an electric field trying to restore the charge difference. This will in turn lead to a oscillatory motion of the plasma particles. The frequency ω_p of the oscillation can, straightforwardly, be derived with the following assumptions (For a more detailed derivations please see [8, p. 71]).

- There is no magnetic field.
- The temperature is 0 K.
- The plasma is infinite.
- The geometry is one-dimensional.
- The ions are stationary.

The last assumption is motivated by the fact that the acceleration of the electrons will, according to Newton's second law of motion, be approximately 2000 times stronger.

Furthermore, the continuity equation

$$\frac{\partial \rho}{\partial t} + \Delta \cdot \mathbf{j} = 0 \tag{2.1}$$

where ρ is the amount of electrons and j is the electron flux, will be vital in our derivation. Note that it is assumed there is no charge creation, which says that we assume no atoms will be ionised and increase the amount of electrons.

The equation of motion for the electrons can be written as

$$m_e n_e \left[\frac{\partial \mathbf{v}_e}{\partial t} + (\mathbf{v}_e \cdot \nabla)\mathbf{v}_e \right] = -e n_e \mathbf{E} \tag{2.2}$$

where m_e is the electron mass, n_e is the electron density, $\mathbf{v}_e$ the electron velocity, $\mathbf{E}$ the electric field and e the electron charge. Equation (2.1) becomes

$$\frac{\partial n_e}{\partial t} + \nabla \cdot (n_e \mathbf{v}_e) = 0. \tag{2.3}$$

With Poisson's equation, one writes

$$\nabla \cdot \mathbf{E} = \frac{\partial \mathbf{E}}{\partial \mathbf{x}} = \frac{e(n_i - n_e)}{\epsilon_0} \tag{2.4}$$

where n_i is the ion density. By linearising the variables:

$$n_e = n_0 + n_1, \quad \mathbf{v}_e = \mathbf{v}_0 + \mathbf{v}_1, \quad \mathbf{E} = \mathbf{E}_0 + \mathbf{E}_1. \tag{2.5}$$

Further more assuming that the plasma from the beginning was neutral and at rest and with small perturbations, $\nabla n_0 = \mathbf{v}_0 = \mathbf{E}_0 = 0$ and $\frac{\partial n_0}{\partial t} = \frac{\partial \mathbf{v}_0}{\partial t} = \frac{\partial \mathbf{E}_0}{\partial t} = 0$. One can rewrite the equation of motion for the electron

$$m_e \frac{\partial \mathbf{v}_1}{\partial t} = -e\mathbf{E}_1 \tag{2.6}$$

where the term $(\mathbf{v}_1 \cdot \nabla)\mathbf{v}_1$ is set to zero since it is quadratic (remember $\mathbf{v}_1$ is small). By treating the continuity equation the same way one gets

$$\frac{\partial n_1}{\partial t} + n_0 \nabla \cdot \mathbf{v}_1 = 0. \tag{2.7}$$

Poisson's equation can now be written as

$$\nabla \cdot \mathbf{E}_1 = \frac{-en_1}{\epsilon_0}. \tag{2.8}$$

Note that it is assumed that $n_0^{ion} = n_0^{electron}$ and $n_1^{ion} = 0$ since the ions, in our model, are stationary. Finally, assuming the plasma wave can be described by $e^{i(kx-\omega t)}$. Equations (2.6 - 2.8) can now be written

$$-im_e \omega v_1 = -eE_1 \tag{2.9}$$

$$-i\omega n_1 = -n_0 ikv_1 \tag{2.10}$$

$$ikE_1 = -\frac{en_1}{\epsilon_0}. \tag{2.11}$$

Solving for ω, one gets the plasma frequency

$$\omega = \boxed{\omega_p = \sqrt{\frac{n_0 e^2}{\epsilon_0 m_e}}} \tag{2.12}$$

which is the non-relativistic formula for the plasma frequency [8, p. 73]. For the relativistic version, the same formula holds except one has to use the relativistic mass. Deriving this is beyond the scope of this thesis.

It is interesting to note that the frequency ω is independent of the wave vector k. This means that with a plasma oscillation alone, a wavelength can not be defined. Thus, when one talks about a plasma wave, the wavelength is given by the speed of the displacement source.

2.3 Electromagnetic waves in vacuum

The plasma density waves studied in this thesis are driven by short laser pulses on the femtosecond time scale. Up to the interaction point, the laser

pulses propagates in vacuum and are described by Maxwell's equations. In this section only the electric field is considered.

The simplest solution to Maxwell's equations in vacuum is the plane wave $E(\mathbf{x}, t)$, described by

$$E(\mathbf{x}, t) = E_0 \cos(\omega t - \mathbf{k} \cdot \mathbf{x}) \tag{2.13}$$

where ω is the angular frequency and $\mathbf{k}$ is the wave vector.

However, a focused laser pulse, where the beam is confined both in space and time, is typically approximated by what is called a Gaussian pulse, described by

$$E(r, x) = \frac{E_0}{2} \frac{W_0}{W(x)} \exp\left(-\frac{r^2}{W^2(x)}\right) \exp\left(-ikx - ik\frac{r^2}{2R(x)} + i\phi(x)\right) f(t). \tag{2.14}$$

Here, W_0 is the beam waist, W is the beam radius at x, r is the distance from the propagation axis, R is the radius of curvature for the phase and $f(t)$ is the temporal envelope of the pulse. ϕ is the Gouy phase.

For the purpose of this thesis, the intensity $I(r, x)$ of the pulse is more interesting. It can be written as

$$I(r, x) = I_0 \left[\frac{W_0}{W(x)}\right]^2 \exp\left[-\frac{2r^2}{W^2(x)}\right] f(t). \tag{2.15}$$

where $f(t)$ is the pulse shape in time.

A measure in the scientific field commonly used to describe the field strength of a laser pulse is the normalised vector potential a_0

$$a_0^2 = \frac{I_0 \lambda_0^2}{2\pi\epsilon_0 c^3}. \tag{2.16}$$

where I_0 is the maximum intensity, λ_0 is the wavelength, c is the speed of light in vacuum and ϵ_0 is the permittivity in vacuum. In a more practical manner it can be calculated by

$$a_0 = 0.85 \lambda_0^2[\mu\text{m}] \sqrt{I_0[10^{18}\text{W/cm}^2]}. \tag{2.17}$$

a_0 relates the driving strength of the electric field to the relativistic mass of the electron. For example, a laser pulse with $a_0 = 1$ drives electrons to quiver with a kinetic energy equal to that of its mass ($m_e c^2$). This means that the physics involved is relativistic.

2.4 Electromagnetic waves in plasmas

LWFA is a laser-plasma interaction phenomenon, and in this section the propagation of laser pulses in plasmas are discussed.

The propagation of an electromagnetic wave in a plasma is described by the dispersion relation [8, p. 102]

$$\omega^2 = \omega_p^2 + c^2 k^2. \tag{2.18}$$

where ω is the driving (laser) frequency, ω_p is the plasma frequency defined earlier. Solving for the wave vector k:

$$k_p = \frac{\sqrt{\omega^2 - \omega_p^2}}{c} \tag{2.19}$$

and note that for $\omega_p > \omega$, k becomes imaginary. This means that an electromagnetic wave can not propagate in a plasma with $\omega_p > \omega$. The threshold density for this is called the critical density n_c and can easily be derived to be

$$n_c = \frac{m_e \epsilon_0 \omega^2}{e^2}. \tag{2.20}$$

Here, a few interesting things happen. Using the dispersion relation (Equation 2.18) it is possible to calculate the phase velocity, $v_{ph} \equiv \frac{\omega}{k}$, of the electromagnetic wave

$$v_{ph} = \sqrt{c^2 + \omega_p^2/k^2} \tag{2.21}$$

which is greater than the speed of light in vacuum! This is allowed since information and energy travel with the group velocity, thus Einstein's theorem still holds. The phase velocity is the velocity at which the phase of one any one component of the wave is moving. For example, a pure sinusoidal wave does not convey information.

The group velocity, $v_g \equiv \frac{d\omega}{dk}$, of the electromagnetic wave is

$$v_g = \frac{c^2 k}{\sqrt{\omega_p^2 + c^2 k^2}} = c\sqrt{1 - \frac{n_e}{n_c}}. \tag{2.22}$$

Recalling the discussion at the end of Section 2.2 note that $v_{ph}^p = v_g^{EM}$. This allows us to define a plasma wavelength λ_p

$$\boxed{\lambda_p = 2\pi \frac{v_{ph}^p}{\omega_p}}. \tag{2.23}$$

For typical electron density values of $10^{18} - 10^{19}$ cm^{-3} and a laser wavelength of 800 nm, λ_p spans from 10 to 33 μm.

An interesting side note is the fact that $v_g < c$ can be seen as photons gaining mass when entering a plasma. The following relation holds for all particles

$$E^2 + p^2c^2 = m^2c^4. \tag{2.24}$$

where E is the total energy of the particle, p is the momentum, and m is the mass. For a photon, $E = \hbar\omega$ and $p = \hbar k$. Thus for free space Equation (2.24) shows that $m = 0$. In a plasma however, inserting E and p and $k^2c^2 = \omega^2 - \omega_p^2$, Equation (2.24) becomes

$$\hbar^2\omega^2 - \hbar^2(\omega^2 - \omega_p^2) = m^2c^4 \tag{2.25}$$

which results in $m = \hbar\omega_p/c^2 \neq 0$.

2.5 Pondermotive force

Another key concept in laser wakefield theory is the pondermotive force. A derivation of this can be found in [8, p. 256] and a brief version is repeated here. The pondermotive force in LWFA is responsible for the displacement of electrons as the laser pulse propagates. Typical values for the laser pulse in a LWFA-lab is $a_0 > 1$ which corresponds to intensities $> 10^{18}$ W/cm^2. This means the effect is highly relativistic, please note that this derivation is classical, but it still gives insight in how the process works.

Consider an electron in an oscillating electric field

$$m_e\frac{d\mathbf{v}}{dt} = -e[\mathbf{E}(\mathbf{r}) + \mathbf{v} \times \mathbf{B}(\mathbf{r})]. \tag{2.26}$$

Note that the $\mathbf{v} \times \mathbf{B}$ is of second order nature. Looking at the first order components, only the electric field is present. The varying electric field can be described by

$$\mathbf{E} = \mathbf{E}_s(\mathbf{r})\cos(\omega t). \tag{2.27}$$

Working with the above equation, one gets

$$m_e\frac{d\mathbf{v}_1}{dt} = -e\mathbf{E}(\mathbf{r_0}) \tag{2.28}$$

$$\mathbf{v}_1 = -(e/m_e\omega)\mathbf{E}_s\sin(\omega t) \tag{2.29}$$

$$\delta\mathbf{r}_1 = (e/m_e\omega^2)\mathbf{E}_s\cos(\omega t). \tag{2.30}$$

This describes the quiver motion of the electrons caused by the oscillating field. Proceeding to second order and expanding the electric field

$$\mathbf{E}(\mathbf{r}) = \mathbf{E}(\mathbf{r_0}) + (\delta\mathbf{r}_1 \cdot \nabla)\, E|_{r=r_0} + \dots \tag{2.31}$$

Rewriting the term $\mathbf{v_1} \times \mathbf{B_1}$ with Maxwell's equation $\nabla \times \mathbf{E} = d\mathbf{B}/dt$ one gets

$$B_1 = -\frac{1}{\omega}\nabla \times \mathbf{E_s}\,|_{r=r_0} \sin(\omega t). \tag{2.32}$$

The second order equation of motion becomes

$$m_e \frac{d\mathbf{v}_2}{dt} = -e[(\delta\mathbf{r}_1 \cdot \nabla)E + \mathbf{v_1} \times \mathbf{B_1}] \tag{2.33}$$

which, inserting equations 2.30, 2.32 into the equation above and time averaging becomes

$$\mathbf{f_{PM}} \equiv m_e \left\langle \frac{d\mathbf{v_2}}{dt} \right\rangle = -\frac{e^2}{2m_e\omega^2}\left[(\mathbf{E_s} \cdot \nabla)\mathbf{E_s} + \mathbf{E_s} \times (\nabla \times \mathbf{E_s})\right] \tag{2.34}$$

where $\mathbf{f_{PM}}$ is defined. The second term can be written as the sum of two terms according to $(\mathbf{A} \times (\mathbf{B} \times \mathbf{C}) = \mathbf{B}(\mathbf{A} \cdot \mathbf{C}) - \mathbf{C}(\mathbf{A} \cdot \mathbf{B}))$. One term cancels the $(\mathbf{E_s} \cdot \nabla)\mathbf{E_s}$ term. Because the average over a period of $\cos^2 x = \sin^2 x = \frac{1}{2}$, one gets

$$\mathbf{f_{PM}} = -\frac{e^2}{4m_e\omega^2}\nabla E_s^2. \tag{2.35}$$

This is the force on a single electron. For a density n_0 written in terms of equation 2.12 the pondermotive force becomes

$$\boxed{\mathbf{F_{PM}} = -\frac{\epsilon_0}{4}\frac{\omega_p^2}{\omega^2}\nabla \left\langle E^2 \right\rangle}. \tag{2.36}$$

Analysing Equation (2.35) one notices that, the force is independent of the sign of the charge, this means both electrons and ions will be pushed away from the laser pulse. The force is inversely proportional to the mass, which, in accordance with Newton's second law, means that the electron will accelerate m_p^2/m_e^2 more than protons! Furthermore there is no polarisation dependence, or in other words, even though the driving laser field is polarised, the pushed electrons will not have a preferred direction.

2.6 Electron density waves driven by a laser pulse

Adding together previous sections, a laser pulse moving in a plasma will push the plasma electrons out of its path. Assume a small density ($n_1/n_0 \ll 1$) perturbation Δn given by

$$\Delta n = n_1 \cos(k_p x - \omega_p t) \tag{2.37}$$

where k_p is given by the group velocity of the electromagnetic field. By integrating Poisson's equation, the electric field can be obtained:

$$\Delta E = -E_0 \frac{n_1}{n_0} \sin(k_p x - \omega_p t). \tag{2.38}$$

The electric field and plasma density relation for a linear electron density wave is illustrated in Figure (2.1)

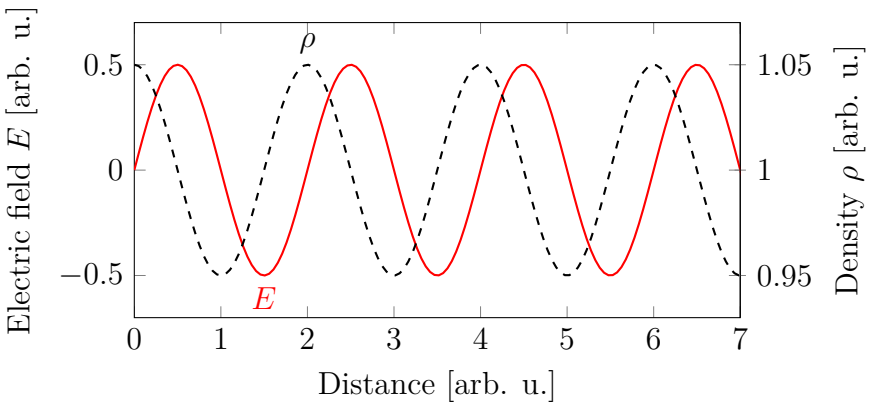

Figure 2.1: The electric field follows the density modulation with a phase delay of $\pi/2$.

If the laser pulse is strong enough electrons will vacate, leaving a plasma wave in the wake of the laser. In Figure (2.2) one can see a crossection of the electron density in the middle of a wakefield. The electrons will experience a strong electric field formed by the remaining ions, pulling them back to the middle. Even though the electrons are accelerated by a strong electric field, it takes them some time to return, creating electron voids behind the laser pulse, as they oscillate back and forth in a transversal movement.

The lack of electrons in the wake of the laser pulse above give rise to a strong longitudinal electric field as seen in Figure (2.2). This wakefield can

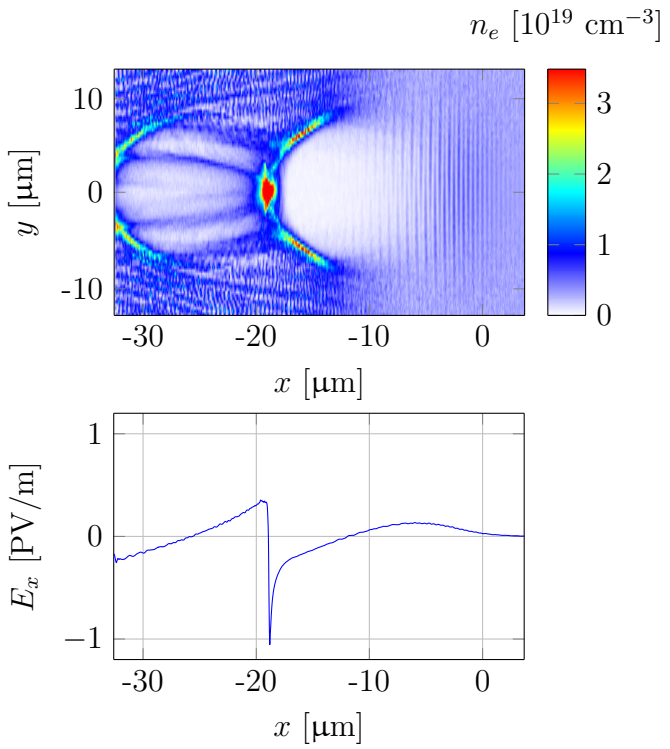

Figure 2.2: Top: A cross section of the circular plasma wave in LWFA. Electron density voids, commonly called bubbles, are formed behind the laser pulse, located at $x = 0$ µm, propagating in positive x-direction, as the returning electron oscillate. Bottom: The x-component of the electric field on the optical axis of the bubble seen above. Note the scale on the y-axis is GV/m. The field within the bubble goes from positive, to 0, to strongly negative.

become strong before it breaks down, much stronger than the conventional RF-cavity. If a test electron were to be placed near the peak electric field in the wake it could be accelerated to high energies over short distances.

There are a few important effects here worth noticing. The laser pulse travels with a finite velocity below c since it is propagating through a medium as described in Section 2.4. An electron with high enough energy can therefore move faster than the light pulse, resulting in a change of the experienced electric field. For example, the group velocity of a laser pulse with a center wavelength of 800 nm traveling in a plasma with a density $n_e = 5 \cdot 10^{18}$ electrons/cm^3 is $v_g = 0.9986c$ according to Equation (2.22). An electron with the same velocity would have an energy of 13 MeV. If the electron comes close enough to the pulse, it will start to decelerate due to the fact it will feel a stronger attraction to the sum of the ions behind it. This can be seen in

Figure (2.2) as the electric field is positive close to the position of the laser pulse. The length the electron has to be accelerated to reach this point is called the dephasing length. This quantifies the limit on the maximum energy an electron can gain for specific laser pulse and plasma density parameters.

2.7 Injection and trapping

In order to be accelerated, electrons have to be placed within the wakefield presented in Figure (2.2), the data for this figure has been produced in CALDER-CIRC, presented in Chapter 3. As mentioned before, today's challenge in this research field is to create a controlled, stable electron beam, in addition to getting to higher energies. The challenging part is to get controlled injection of electrons, into the wakefield, localised in space and time, thus controlling the electron energy.

The most common and experimentally first achieved method for injecting and trapping of electrons in the plasma wave is called self-injection. This happens when the plasma wave is driven strong enough. It is achieved by letting a laser pulse propagate in a high enough density (relative to the laser parameters) where it will evolve and self-compress, such that the density wave finally breaks which will inject charge. This injection scheme has the main advantage of being experimentally simple. There are a few problems with this scheme however. One being that it is hard to control exactly where along the optical path injection will occur. Another is to control that electrons are only injected at one location in the plasma. A third is to control in which plasma period electrons will be injected. In Figure (2.3) the electron density cross section is illustrated shortly after self-injection has occured.

Another method for injection and trapping of electrons is the colliding pulse scheme [9, 10, 11]. Here, the driving laser pulse collides with another, much weaker, counter-propagating pulse in the plasma. This is well localised both in space and time, resulting in a controlled amount of accelerated electrons and the electron energy. A challenge with this is that it requires extreme precision, since two laser beams, with spot sizes on the order of 10 μm has to collide head-on.

Another method is ionisation injection. [12, 13, 14, 15] In a typical experiment, you either use hydrogen or helium as a plasma base. Both of these gases are fully ionised by the electric field in the wings of the laser pulse. When a heavier element is introduced to the plasma, such as nitrogen, electrons bound strongly will be ionised closer to the pulse peak. If the peak intensity of the laser pulse is matched to the threshold for ionisation of these tightly bound electrons, the electrons will be released into the plasma within

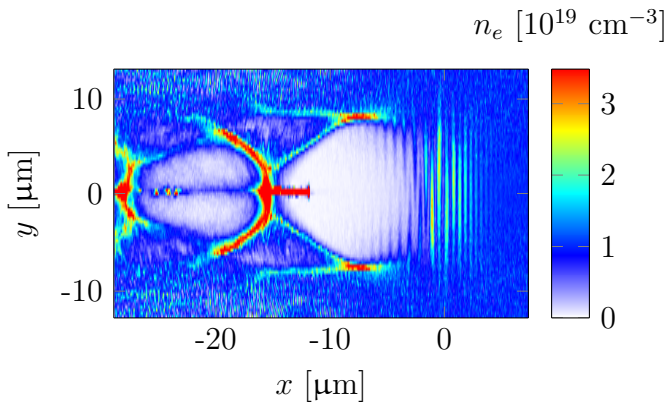

Figure 2.3: Injection due to self-injection by wavebreaking has occured, and charge is injected in the two first plasma periods.

the first plasma period. In a constant density, this method has the same problem as self-injection, but combined with a density modulation it shows promising results [16].

Density down-ramp injection

The method for injection, which this thesis is dedicated to, is density down-ramp injection. It was first proposed by Bulanov et al. [17]. As the laser pulse propagates along a density down-ramp, the bubble expands due to the decreasing plasma frequency, see Figure (2.4). One way to explain this is to look at Equation (2.12) and (2.23). λ_p (and thus the bubble) increases with a decrease in density. During the expansion process, some of the background electrons returning to the optical axis will fall into the expanding bubble. As soon as the electron enters the bubble (from the rear side), it will experience a strong electric field directed towards the center of the density void. This in turn traps the electron at the back of the bubble and it will be hard for it to escape, resulting in injection.

Another way of explaining it is to look at the phase velocity of the wave when the laser goes down the density gradient. The phase velocity v_p of the plasma wave [18] can be described as

$$\frac{v_p}{c} = \left(1 + \frac{x - ct}{k_p}\frac{\partial k_p}{\partial x}\right)^{-1} \tag{2.39}$$

where c is the speed of light in vacuum, x is the position along the x-axis, t is the time the peak of the laser pulse has travelled in the plasma, $k_p = 2\pi/\lambda_p$. According to Equation (2.39) the phase velocity decreases behind the laser

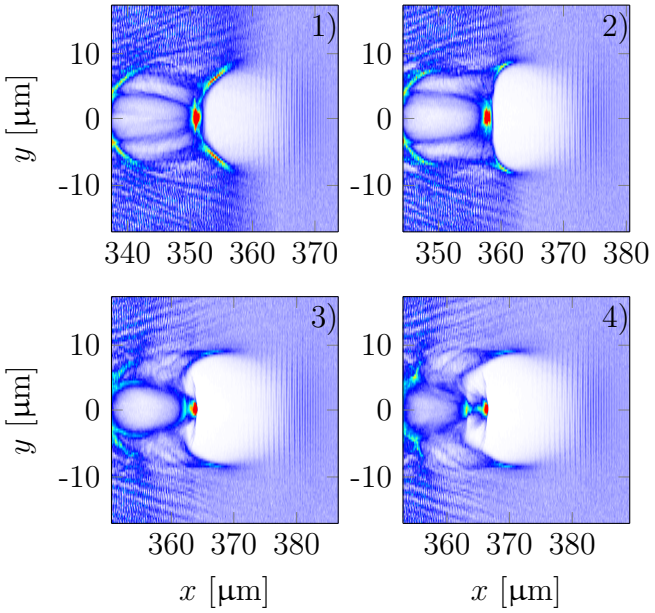

Figure 2.4: The electron density distribution formed by a laser pulse going down a density gradient in four steps. One can see the expansion of the electron density wave which causes the electrons at the back edge to be injected.

pulse ($x - ct < 0$) if its going down a negative density gradient ($\partial k_p / \partial x < 0$). Now the electrons at the back of the wave has a chance to outrun the phase velocity for a short while (as long as the gradient lasts). The electrons with high enough velocity can now be trapped. It is similar to what happens in self-injection, where the electrons instead feel the strong wakefield built up over time and then outruns phase velocity.

In Figure (2.5) a typical example of electrons trapped in a short density gradient (on the order of 10 µm) is shown. In Figure (2.6) one can see a 2D phase-space picture and the energy distribution of the electron bunch.

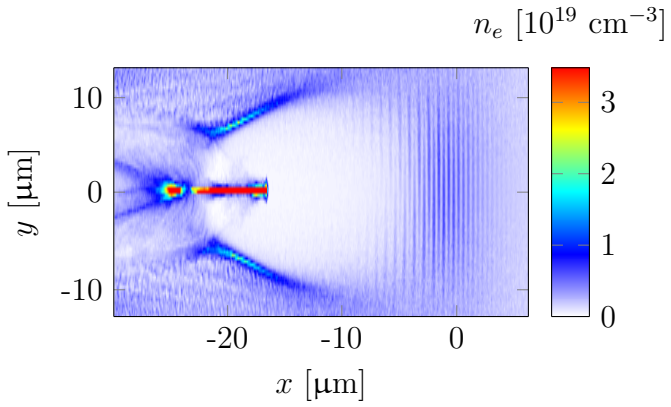

Figure 2.5: A bubble with injected charge that has been accelerated over 500 µm. Note that the bubble is no longer free of electrons.

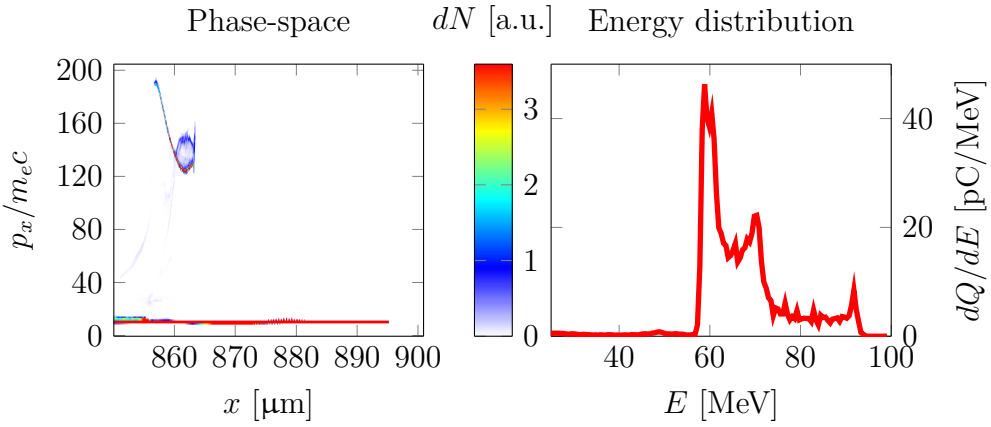

Figure 2.6: To the left a phase-space picture (the momentum plotted against the position) of the charge in Figure (2.5). Injected electrons can clearly be distinguished in phase-space, since they quickly gain energy in the strong electric field within the electron void. The red line at the bottom of the graph represents the background electrons, with a maximum normalised momentum close to a_0. To the right the energy distribution of the accelerated electrons.

Chapter 3

Numerical method

This chapter contains three elements. It introduces the concept of a particle-in-cell (PIC) codes, it describes the features of CALDER-CIRC and describes the cluster used for the simulations. It differs from the other chapters in this thesis since it does not discuss laser wakefield acceleration, only the tool used to simulate the physical process.

3.1 PIC-code

In order to calculate the plasma dynamics Maxwell's equations

$$\begin{aligned}
\nabla \times \mathbf{E} &= -\frac{\partial \mathbf{E}}{\partial t} \\
\nabla \times \mathbf{B} &= \frac{\mathbf{J}}{\epsilon_0 c^2} + \frac{1}{c^2}\frac{\partial \mathbf{E}}{\partial t} \\
\nabla \cdot \mathbf{E} &= \frac{\rho}{\epsilon_0} \\
\nabla \cdot \mathbf{B} &= 0.
\end{aligned}$$

need to be solved. Here $\mathbf{E}$ and $\mathbf{B}$ is the electric and magnetic field, $\mathbf{J}$ the current density, c is the speed of light in vacuum, ϵ_0 the vacuum permittivity and ρ the charge density. In addition Vlasov's equation need to be solved for the kinetic description of the particles

$$\begin{aligned}
\frac{\partial f_e}{\partial t} + \mathbf{v}_e \cdot \nabla f_e - q_e \left(\mathbf{E} + \mathbf{v_e} \times \mathbf{B}\right) \cdot \frac{\partial f_e}{\partial \mathbf{p}} = 0 \\
\frac{\partial f_i}{\partial t} + \mathbf{v}_i \cdot \nabla f_i + q_i \left(\mathbf{E} + \mathbf{v_i} \times \mathbf{B}\right) \cdot \frac{\partial f_i}{\partial \mathbf{p}} = 0
\end{aligned}$$

where f_α is $f_\alpha(\mathbf{x}, \mathbf{p}, t)$ the distribution function for the specie α as a function of space, momentum and time, q_e is the absolute value of the electron charge, q_i is the charge of the ions and $\mathbf{v}_\alpha$ is the velocity for the specific specie. The

following relations can be used to calculate ρ, $\mathbf{J}$ and $\mathbf{v}_\alpha$

$$\rho = q_e \int (Z_i f_i - f_e) d^3p$$
$$\mathbf{J} = q_e \int (Z_i f_i \mathbf{v_i} - f_e \mathbf{v_e}) d^3p$$
$$\mathbf{v}_\alpha = \frac{\mathbf{p}}{m_\alpha \sqrt{\left(1 + \frac{p^2}{(m_\alpha c)^2}\right)}}.$$

where $Z_i = q_i/q_e$.

Vlasov's equation provides a more general description of a plasma than a fluid model (i.e. magnetohydrodynamics) and can therefore handle extreme conditions better. However, Vlasov's equation itself does not include particle collisions.

Solving this set of equation for every particle in a plasma would be computationally impossible with today's computer. Instead, in a PIC-code, one solves the field equations with a finite difference method on nodes that together form a mesh. The particle dynamics are solved by bunching physical particles into larger macro particles who represent the physical particles by carrying the sum of their charge and mass. The equations are then solved iteratively with discrete time step. This process can be described in four main steps, visualised in Figure (3.1). In practice, more advanced schemes are used to get higher order precision and avoid certain numerical difficulties, but the basic process remains the same.

The coupling between Maxwell's equations and Vlasov's equation is done in two steps. From the particles to the field through projection of the charge and current onto the mesh. A linear model for this is presented in Figure (3.2). From the field back to the particles through an interpolation scheme between the different nodes to calculate the fields at the particles position.

Due to the nature of this model, it can not reproduce microscopic phenomena of a plasma, or rather, phenomena smaller than you choose to resolve. If too few particles are used in the simulations, a number of discretisation effects and numerical errors will occur further discussed in i.e. [19]. A rule of thumb is that one needs a fair amount of particles per minimum length in the plasma that you want to resolve, which in the case of this study, would be the laser wavelength. To check that the resolution is good enough, one can run two simulations, one with twice the amount of particles as the other. If there is a significant difference in the results, more particles and/or a finer mesh is needed.

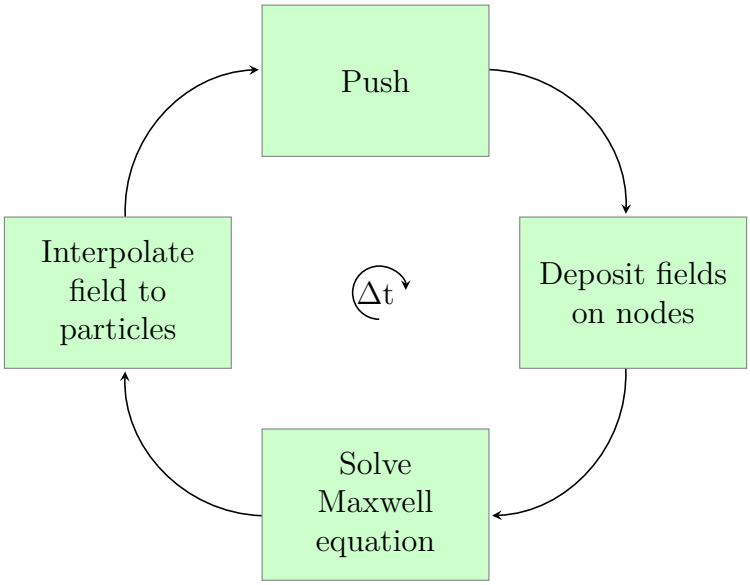

Figure 3.1: A typical PIC-code time-step loop. The existing field is used to integrate the equation of motion for the particles, the electric fields and currents are then calculated and deposited on the grid. Maxwell's equations are solved on the finite difference form and the advanced fields are then interpolated to the particles and the cycle starts over again. [19]

3.2 CALDER-CIRC

3D PIC-codes are computationally heavy and even with a state of the art super computer you can only run so many simulations. For the numerical studies in this report the PIC-code CALDER-CIRC [20] was used. CALDER-CIRC is specifically developed to simulate LWFA and is fully relativistic. It exploits the cylindrical symmetry of wakefield acceleration and uses Fourier decomposition of the electric field to reduce the computing time by up to two orders of magnitude, compared to a full 3D code.

In laser wakefield acceleration, the physics happens very close to the optical axis. The mesh in CALDER-CIRC is defined in radial coordinates, the further away from the optical axis a mesh box is, the greater the volume. Each box contains the same number of macro particles. This results in a decrease in resolution along the radial axis (due two the lower amount of particles) which has the benefit of a reduction in the the computational load of the particle pusher.

CALDER-CIRC also has a moving window option, where you only simulate the plasma close to the laser pulse. This of course, also saves a lot of computing power.

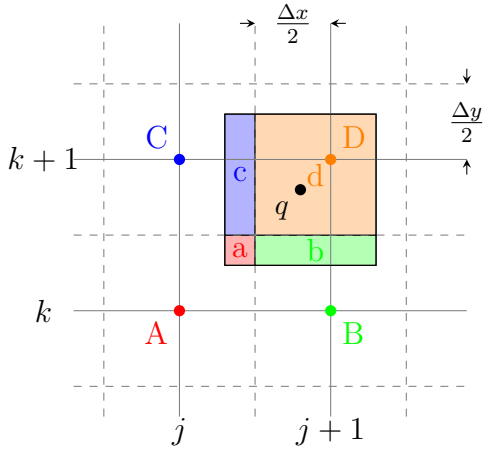

Figure 3.2: Linearly weighted charge assignment in two dimension for a particle (the black dot) with charge q. a charge proportional to the the area $a/(\Delta x \Delta y)$ is assigned to node A etc. Since node D is the closest to the charge, it is assigned most of the charge. [19].

An input file example can be found in Appendix B and a description of the output files can be found in Appendix C.

Fourier decomposition of the laser field

[20] writes that the fields of a cylindrical symmetric polarised laser pulse can be described with the following equations in three dimensions

$$\mathbf{E}(\mathbf{r}, \mathbf{x}, \theta, \mathbf{t}) = E_y(r, x, t)\hat{y} = E_y(r, x, t)(\cos(\theta)\hat{e}_r - \sin(\theta)\hat{e}_\theta) \tag{3.1}$$

$$\mathbf{B}(\mathbf{r}, \mathbf{x}, \theta, \mathbf{t}) = B_z(r, x, t)\hat{z} = B_z(r, x, t)(\sin(\theta)\hat{e}_r + \cos(\theta)\hat{e}_\theta) \tag{3.2}$$

where $r = \sqrt{y^2 + z^2}$. The fields can be decomposed into a Fourier series

$$\mathbf{F}(r, x, \theta) = \mathbb{R}\left(\sum_m \hat{\mathbf{F}}^{\mathbf{m}}(r, x)e^{-im\theta}\right) \tag{3.3}$$

which is an infinite sum. However, it turns out that one only need to calculate a few modes in order to represent the physics of LWFA well. Note, for example, that the field-components of a wakefield is axisymmetric and is represented well by the $m = 0$ mode and that a linearly polarised laser pulse can be reproduced fully with a $m = 1$ mode. Thus, with 2 modes, both the laser field and wakefield can be represented. This description of the laser pulse is needed when interpreting the output files described in Appendix C.

Courant–Friedrichs–Lewy condition

In order to keep the numerical solutions to differential equations convergent the Courant–Friedrichs–Lewy (CFL)-condition must be fulfilled. The CFL-condition puts a condition on the maximum time step allowed, which depends on the grid size. The specific condition varies depending on your solver. For CALDER-CIRC, there are two different field-solvers to choose from. The standard Maxwell solver and the anti numerical Cherenkov scheme, which was implemented to avoid numerical Cherenkov radiation. the following conditions apply:

If the anti numerical Cherenkov scheme is used, the CFL-condition in normalised units is

$$\mathrm{d}t < \mathrm{d}x \tag{3.4}$$

where $\mathrm{d}t$ is the time step and $\mathrm{d}x$ is the longitudinal grid size. If the standard Maxwell solver is used, the CFL-condition is

$$\mathrm{d}t < \frac{1}{\sqrt{1/\mathrm{d}x^2 + m^2/\mathrm{d}r^2}} \tag{3.5}$$

where $\mathrm{d}r$ is the radial grid size and m is the highest order m-mode used in the simulation i.e. if one uses the first three modes (0,1,2) m will be 2.

Scalability

CALDER-CIRC scales well with a growing number of cores, presented in Table (3.1). This test was performed by Xavier Davoine on up to 8192 cores on TERA100 at CEA-DIF using a cylindrical mesh of 25,600 x 2,560 cells in the longitudinal and transverse directions.

#cores	Speedup
256	1.00
512	1.98
1024	3.89
2048	7.13
4096	12.6
8192	18.3

Table 3.1: Speedup table for CALDER-CIRC. The measured speedup is normalised to running the code on 256 cores. As can be seen, the code scales well with an increasing amount of cores. For jobs running on up to 1000 cores it scales almost linearly.

Normalisation

In the code, all physical quantities are normalised according to Table (3.2). Normalisation is used to simplify equations in the code since most physical constants will disappear. It also keeps results easy to compare, for example something moving with the velocity of light will travel 100 length units in 100 time units. Since the code is tracking relativistic electrons and laser pulses this feature comes in handy. Another example is that the vector potential of the laser field is on the order the transverse momentum of the electrons it pushes.

Physical quantity	Normalisation
Time	$1/\omega_0$
Distance	c/ω_0
Velocity	c
Mass	m_e
Charge	e
Momentum	$m_e c$
Density	n_c
Vector potential	$m_e c/e$
Electric field	$m_e c\omega_0/e$
Magnetic field	$m_e \omega_0/e$
Number of particles	$n_c(c\omega_0)^3$

Table 3.2: Normalisation table, c is the speed of light, ω_0 is the angular laser frequency, m_e is the electron mass and e is the electron charge.

3.3 Simulations

A total of 400 000 CPU-hours (one CPU-hour is one hour on one core) has been used to run the simulations. The simulations were typically running on 400 cores in parallel, and a total of 35 simulations has been used for this thesis project.

All simulations were conducted at the Alarik cluster at Lunarc, Lund University. Alarik has 208 nodes and 3328 processors (cores) at 3.0 GHz with typically 4 Gb of memory per core. It has a local storage on each node, and the job submission script and the source code had to be modified to utilise these.

Chapter 4

Experimental method

An experimental setup used for LWFA is described. The top-view diagnostic looking at Thomson scattered light which is improved as part of this project, is evaluated and discussed in more detail.

4.1 Multi-Terawatt Laser system at Lund Laser Centre

The Multi-Terawatt Laser system at the Lund Laser Centre is a titanium sapphire (Ti:Al_2O_3) based chirped pulse amplification (CPA) system. A schematic illustration of the laser can be seen in Figure (4.1).

The CPA-system starts in an oscillator producing 80 million 25 fs pulses per second.

According to Fourier theory, a short pulse contains a broad range of frequencies. This effect is used to stretch the pulse in time. Different wavelength components are engineered to be split into different optical paths, and when gathered again in the end, the pulse is stretched.

The pulse is then amplified, from the order of a nJ in the oscillator to a J in the end by passing through a series of amplifiers.

Before being sent to the target, the pulse is compressed again, by the reverse method used to stretch it.

For these experiments presented in this thesis, the final pulse is approximately 35 fs long and contains 0.65 J at the target.

4.2 Experimental setup

The laser pulses described in the previous section are sent to the experimental chamber. A gas cell with an adjustable length is used as a gas container for the target. It is described in Figure (4.2). Gas is filled into the cell from a reservoir at a pressure controlled using an electronic regulator. At the

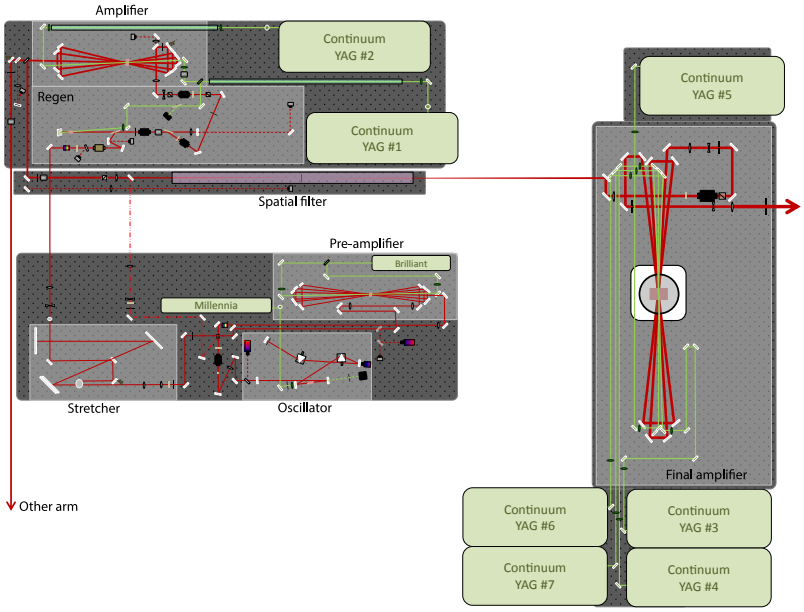

Figure 4.1: A schematic picture of the Multi-Terawatt Laser system at Lund Laser Center. Short pulses are born in the oscillator, and after that they are stretched. The rest of the system contains a series of different amplifiers, ramping up the energy.

entrance and exit, sapphire windows with a hole are placed to let the laser pulse through. On the sides of the cell, windows are mounted to be able to look at the Thomson scattered light.

A parabolic mirror with a focal length of 75 cm was used to focus the laser pulse to a 18 μm FWHM spot size. The pulse then reaches an intensity of $4 \cdot 10^{18}$ W/cm^2 which corresponds to $a_0 = 1.3$. A sketch of the setup can be seen in Figure (4.3) The laser energy was kept at 0.6 J per pulse at the target, with a pulse duration of 35 fs. A scintillating screen was used to detect electrons. A dipole magnet was used to determine the electron energy spectra of the bunches of accelerated electrons. When the electron bunch travel through the magnet, the amount their path is bent will depend on the energy of the incoming electron. A highly energetic electron, due to relativistic mass effect, will bend less when experiencing the force from the magnetic field, and will therefore be accelerated less downwards, compared to an electron with lower energy. The electrons are then split into an energy spectrum on the scintillating screen, which can then be translated into energy if one has a reference value.

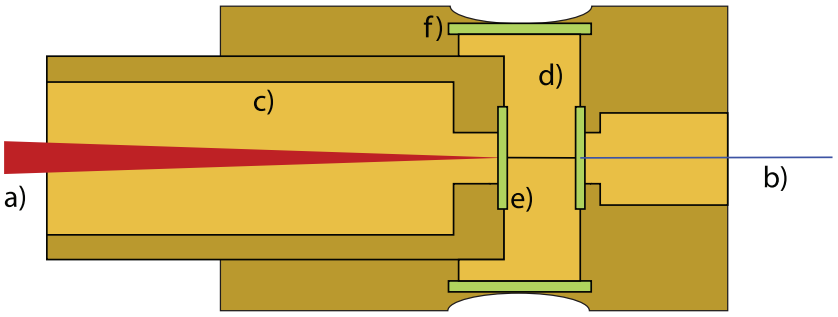

Figure 4.2: The gas cell to contain the interaction gas medium. a) The incoming laser beam, b) the outgoing electrom beam, c) adjustable piston, d) gas container, e) entrance sapphire window, f) optical sapphire window. The length of the gas cell can be varied with the help of the piston. Two sapphire windows each with a 100 µm hole in the center forms the entrance and exit for the laser and electron beams. There are three optical windows in the gas cell for optical diagnostics of the interaction. In addition to the two seen in the figure, there is an additional one on the top which was used in the top-view setup.

Figure 4.3: Sketch of the experimental setup. a) Parabolic mirror, b) laser beam, c) gas cell, d) electrom beam, e) dipole magnet, f) dispersed electron beam, g) scintillating screen. The laser pulse is focused into the gas cell. Laser wakefield acceleration of electrons takes place in the cell. The electrons exit from the gas cell to the right traveling into a spectrometer.

Laser focus

With the help of the deformable mirror, the lasers intensity profile could be modified. Two profiles used are presented in Figure (4.4).

4.3 Top-view diagnostics

Thomson scattered light

A free charged particle that interacts with an oscillating electric field will start an oscillating motion. This oscillating motion will involve acceleration, and the particle will therefore emit light. This can also be viewed as scattering of

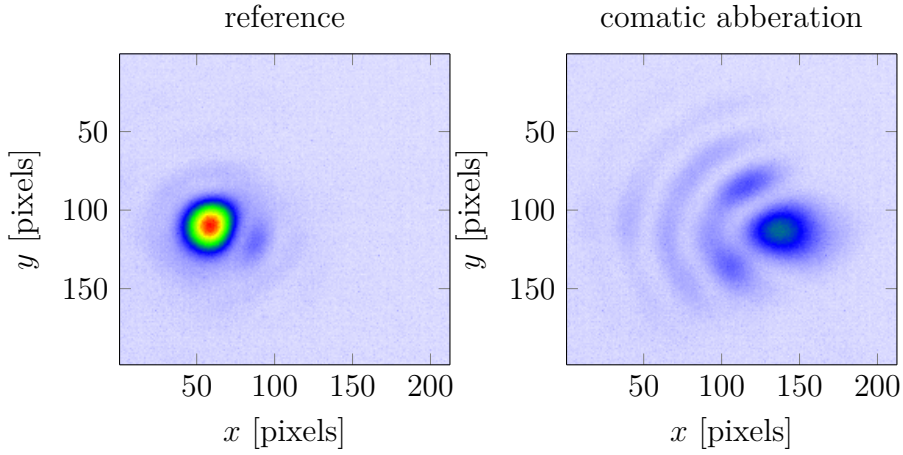

Figure 4.4: A reference intensity profile and one with comatic abberation.

light against a charged particle. This is called Thomson scattering and the cross section, which is a measure of the probability that a photon will scatter, σ_T is [21, p. 489]

$$\sigma_T = \frac{8\pi}{3}\left(\frac{e^2}{mc^2}\right)^2. \tag{4.1}$$

The likelihood that light will scatter is inversely proportional to the mass squared! This means that a proton (i.e. the lightest ion) will scatter 4 million times less light than an electron.

The Thomson scattered light in the plane of the detector can be described by the following parameters [22].

$$\Phi_{Thomson}(y,x) \propto \int_y^{+\inf} n_e(r,x)\left|\frac{a_o(r,x)}{\gamma(r,x)}\right|^2 \frac{r}{\sqrt{r^2-y^2}}dr \tag{4.2}$$

where n_e is the electron density, a_o is the vector potential of the laser pulse and γ is the Lorentz factor related to the quiver motion of the electrons. Over a short density down-ramp gradient, one could assume that n_e will be the parameter that changes significantly. Therefore, it could be a possible method to experimentally observe a laser pulse propagating through short density gradient.

Top-view

The top-view setup is used to image the Thomson scattered light from the laser pulse. An improvement in resolution compared to the earlier, one-lens imaging setup was desired. Due to the limited space within the interaction

chamber, and the limited ability of cameras to operate in vacuum, the camera was placed outside the vacuum chamber. Furthermore, the intensity of the Thomson scattered light also varies by several orders of magnitude, requiring a practical way to vary the attenuation in the imaging system.

Principles of relay imaging systems is shown in Figure (4.5b). The object plane coincides with the focal plane of lens L1. Rays from a point source in the object plane will always be parallel in region B. The beam is then focused by lens L2 to it's focal plane, which coincides with the image plane. An effect called vignetting is caused by the fact that, as illustrated with object b, some of the parallel rays going out from L1 misses the focusing lens L2. This has two effects on the image. The intensity of the light reaching the image decreases with the distance between the imaged point and the principal axis. This effect can be seen experimentally in Figure (4.6b), where the edges and corners are dark. Vignetting also decreases the effective aperture of the system when the imaged point is moved away from the principal axis. This affects the resolution and can also be seen in Figure (4.6b). In the center-right part of the picture, the horizontal lines stay sharp further away from the center than the vertical ones. This is due to the fact that the aperture is squeezed more in one of the dimensions. A benefit of the relay imaging system is that it allows for neutral density filters to be placed within region B without affecting the image focus.

A Mitutoyo near-infrared (NIR) microscope objective with a focal length of 20 mm, working distance of 30.5 mm, numerical aperture of 0.26, and a specified resolving power of 1.1 μm was used to get a high resolution. A camera (Allied Vision Pike), with a pixel size of 6.45 μm on the CCD-chip, was used to image the Thomson trace.

To match the optical resolution of the microscope objective with the pixel size, an optical magnification of approximately 5-6 is needed. Therefore, a 100 mm focal length eyepiece was used. The full setup is illustrated in Figure (4.5a).

The resolution was tested for 800 nm light by putting a monochromatic filter on the camera, looking at a backlit copper-wire grid with 1000 wires per inch. The result can be seen in Figure (4.6a) where a resolution of around 2 μm is verified. A problem with high spatial resolution is that the depth of focus also will be short. Using the Rayleigh length to estimate the depth of focus, one get approximately 10 μm. The focused laser pulse driving the wakefield accelerator has a diameter of 18 μm. This means the setup will be sensitive since a small movement of either the laser focus or the microscope objective will move the plasma channel out of the focus plane.

In order to manage this, the camera itself was mounted on a translation stage. Mounting the camera on a translation stage has the advantage of

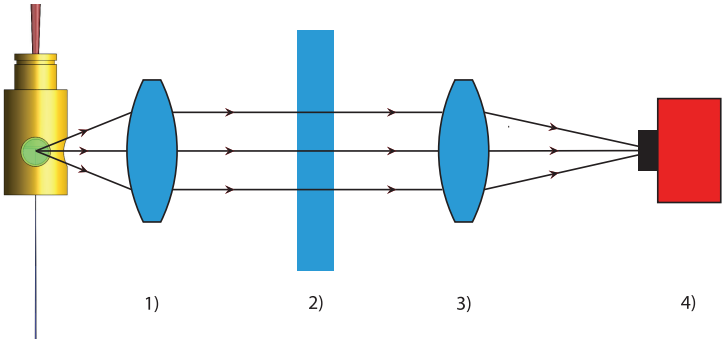

(a) The top-view imaging setup used in the experiment with an estimated resolution of 2 µm. 1) The microscope objective. 2) The optical window that couples the light out from the experimental chamber. 3) The focusing eyepiece. 4) A camera.

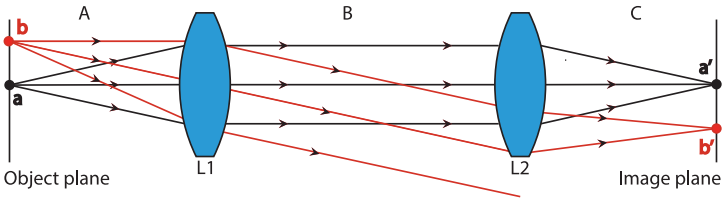

(b) A relay imaging system. Two lenses form an imaging system where the rays are parallel between the two lenses. Vignetting is caused by the fact that for objects not in the center of focus for lens L1, part of the parallel beam will miss the focusing lens.

allowing for a very precise adjustment of the focus , since the translation scales as the magnification of the system squared. This way fine-tuning of the system is easily done.

Vignetting is an effect that has to be considered for a relay imaging system (see Figure (4.5b)). As seen in Figure (4.6b) this effect can reduce the quality and field of view of your image. The effect increases with the distance between the lenses, and it can be reduced by using an eyepiece with larger diameter. Since large lenses with good quality tends to be expensive, the easiest way to avoid this problem is to keep the distance between the microscope objective and the eyepiece as short as possible. Therefore, the camera and eyepiece was mounted on the lid of the experimental chamber itself. This is not practically ideal, since whenever work is done within the chamber, the setup itself moves when we lift off the lid and when we use the vacuum pumps. After this the setup has to be re-aligned.

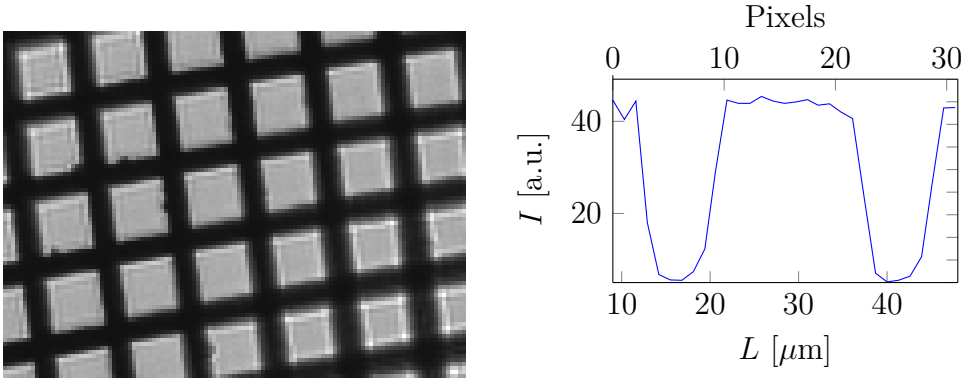

(a) To the right an example picture of the copper grid. To the left an analysis of the resolution. You can see that the intensity drops more than 80 % (and reaches it's lowest point) over two pixels. This indicates that the resolution is less than 2 pixels on the camera, which would correspond to a resolution better than 2.6 µm. An optical resolution close to the extent of 2 pixels would result in a 3 pixel transition unless the pixels and copper grid is perfectly matched.

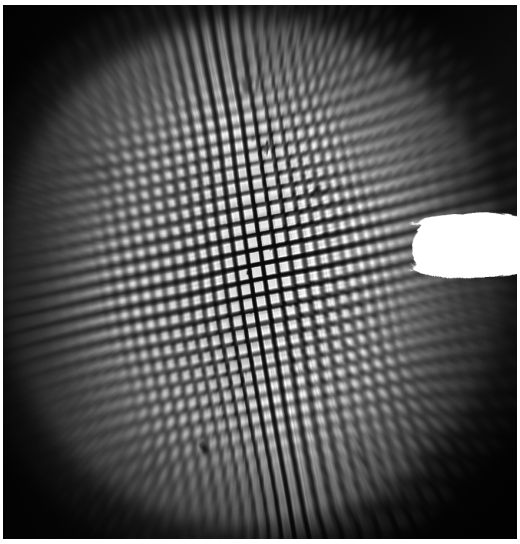

(b) Vignetting can clearly be seen in this picture. Note how the intensity and resolution decreases with the radius. The white spot to the right comes from a burned spot, where intense light has destroyed the pixels on the CCD-chip.

Chapter 5

Result and discussion

The result of the PIC-simulations and laser wakefield acceleration experiments are presented and discussed in this chapter.

5.1 Top-view

This section focuses on the testing and result from the experimental part of this thesis project. Here a test of the top-view setup on a uniform density distribution is presented. However, no actual density down-ramp measurements were made or attempted.

Results and discussion

The longest observed trace of the Thomson scattered light was approximately 400-500 μm long, but in most cases shorter. During the experiment the length of the gas cell was significantly longer (around 3.5 mm) than the scattered light trace we could see. The reason why we do not see the rest is probably due to limits in the dynamic range of the camera. When the pulse first enters the gas, it interacts strongly with the electrons. More importantly, the whole pulse interacts with electrons. As the bubble forms, electrons are pushed away, and a smaller part of the pulse actually get a chance to scatter from the electrons. This reduces the intensity of the scattered light. Since we need to protect the camera with neutral density filters to prevent it from being damaged, the low intensity trace of the Thomson scattered light blocked entirely.

A few general things are worth noticing about the Thomson scattered light. If the acceleration works well, the top-view will yield a relatively low light intensity. This is because when the laser pulse forms a plasma wave that enters the bubble regime, the laser light will not interact as strongly with the electrons, and therefore less light is scattered. For example, if the beam focus plane position is bad, more light will be Thomson scattered, due to the fact

that the laser pulse can not drive a plasma wave.

A typical image of Thomson scattered light can be seen in Figure (5.1).

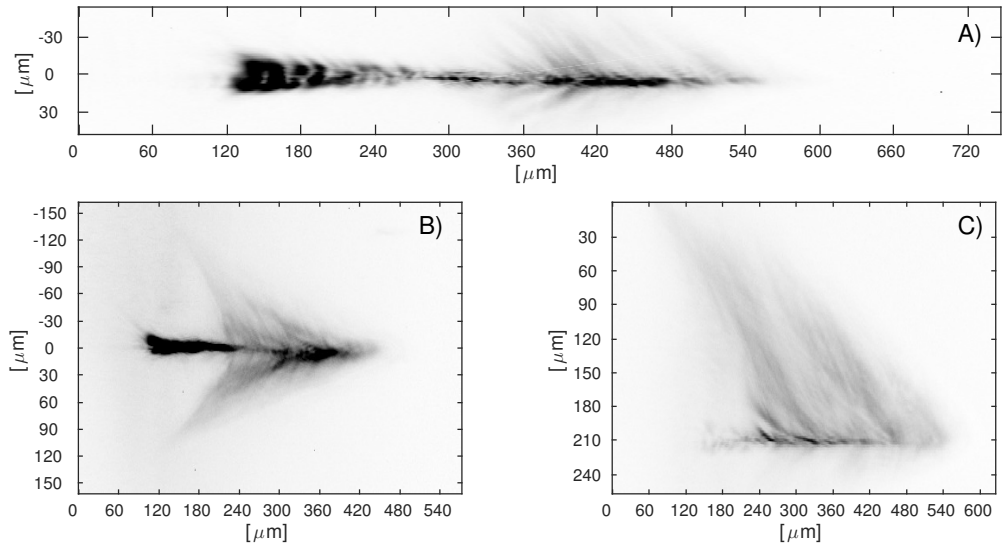

Figure 5.1: A) typical picture of the Thomson scattered light acquired in the experiments. B) A fir tree like shape was seen in the top-view images. C) If the focus has a comatic abberation it becomes a one-sided fir tree instead.

The length of the bright part of the plasma channel was observed to shorten with a higher backing pressure, which is directly proportional to the electron density, see Figure (5.2).

In PIC-simulations one can see that the bubble forms faster when the laser pulse evolve in higher densities, see Figure (5.3). Note how the density within the bubble is lower for the higher density case. Also note that the diameter of the bubble (and therefore the laser pulse's) is significantly smaller in the high density case. The fact that the bright part of the plasma channel gets shorter with an increased backing pressure might seem contra-intuitive since there are more electrons for the laser to scatter on. In a higher density, the relativistic self-focusing of the pulse is stronger. In PIC-simulation, we can see that for a higher electron density, the bubble forms faster, see Figure 5.3. The fact that the bubble gets vacated faster fits well with the fact that this is an initial effect that we see in the beginning of the plasma channel. It should also be noted that the amount of Thomson scattered light depends on the γ-factor of the plasma electron as $\propto a/\gamma$. This indicates that the electrons close to the center of the laser field, do not contribute since they are moving fast and have a high γ-factor.

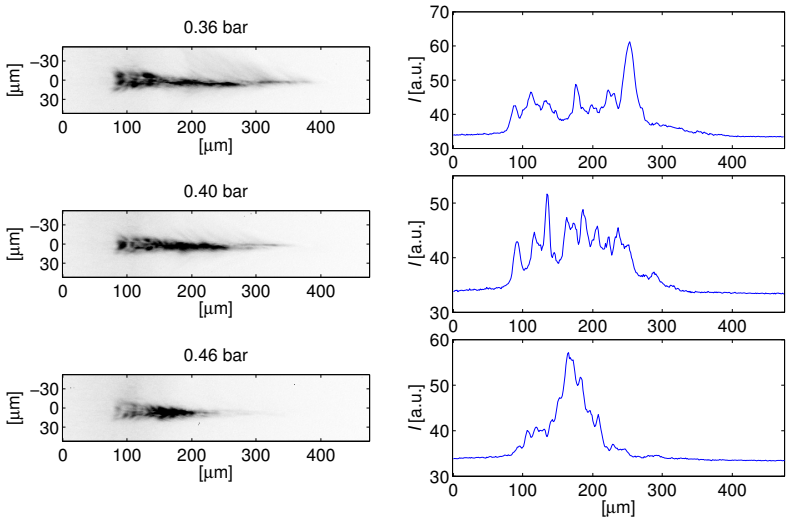

Figure 5.2: Topview images with 3 different backing pressures. To the left you see acquired images, and to the right their respective line outs. Please note that the pictures to the left are not saturated, but brightened to reveal the shape of the channel better.

A fir tree like shape was observed in most the top view images, presented in Figure (5.1). A one sided version could be produced by modifying the focus of the laser to have comatic abberation.

The fir tree shape is peculiar, and a direct cause is hard to pin down without more data. This is the first time a top-view installation is used with this gas cell. It is therefore hard to rule out possible optical effects. One could imagine that this is laser light reflected at the gas cell's entrance through the sapphire plate, returning to the plasma channel, scattering light on its way. This is supported by the fact that it becomes one sided and stronger with a comatic abberation in the focus where more light misses the focus and can be reflected. However, this can with the presented data not be concluded. Another hypothesis is that this is light leaking from the laser pulse, but as it is self-focused, the leak decreases. It is harder to motivate how this would explain the fir tree like shape.

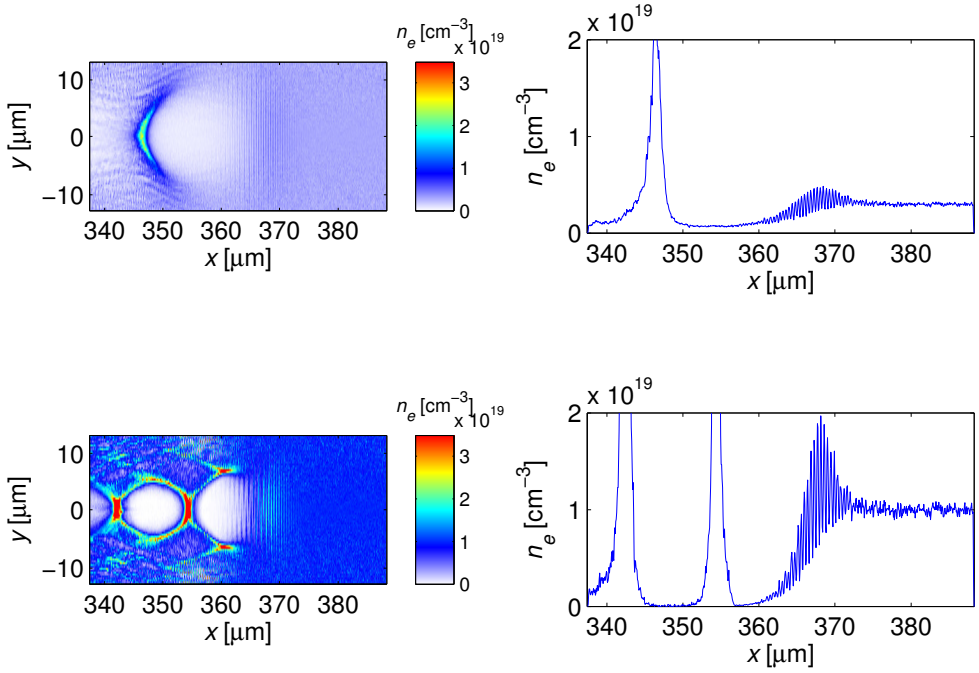

Figure 5.3: PIC-simulations of LWFA with the same laser parameters but two different densities. To the left a density cross section around the laser pulse, to the right a line out of the cross section in the middle. The upper figures corresponds to an electron density of $n_e = 3 * 10^{18}$ cm^{-3} and the lower one $n_e = 10^{19}$ cm^{-3}.

5.2 Studies of density down-ramp injection

This section focuses on the numerical studies on down-ramp injection conducted for this thesis.

In order to make the presentation of the results and the discussion smoother, some terminology is defined in Figure (5.4). The peak density will be referred to as n_{peak}, the lower plateau will be referred to as the acceleration region and the corresponding density n_{acc}, the difference in density between the two regions is $\Delta n = n_{peak} - n_{acc}$, and the length of the density down-ramp as l. Q is the injected charge, E refers to energy and E_x refers to

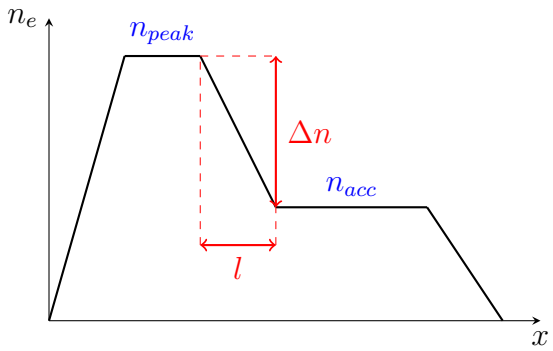

Figure 5.4: The upper density will be referred to as n_{peak}, the lower as n_{acc} as in acceleration, the density difference $\Delta n = n_{peak} - n_{acc}$ and the length of the gradient l

the longitudinal electric field.

Results and discussion

Verification of experimental data

A series of simulations were performed to validate an hypothesis about the injection based on experimental findings.

The experimental setup was the same as the one described in Chapter 4 except for the target. The target consisted of two gas jets, one originating from a 2 mm nozzle providing a broad plateau, and one originating from a 0.4 mm nozzle providing a localised density peak. The total density profile was measured to be the sum of the individual density profiles. This created a density down-ramp followed by an acceleration plateau similar to the one shown in Figure (5.4).

The experimental laser parameters were a FWHM temporal profile of 40 fs, a spatial profile of 19 µm and an $a_0 = 1.3$.

During a scan were the upper plateau density n_{peak} was varied, the data in Figure (5.5) was collected. For density values above $11 \cdot 10^{18}$ cm^{-3} the

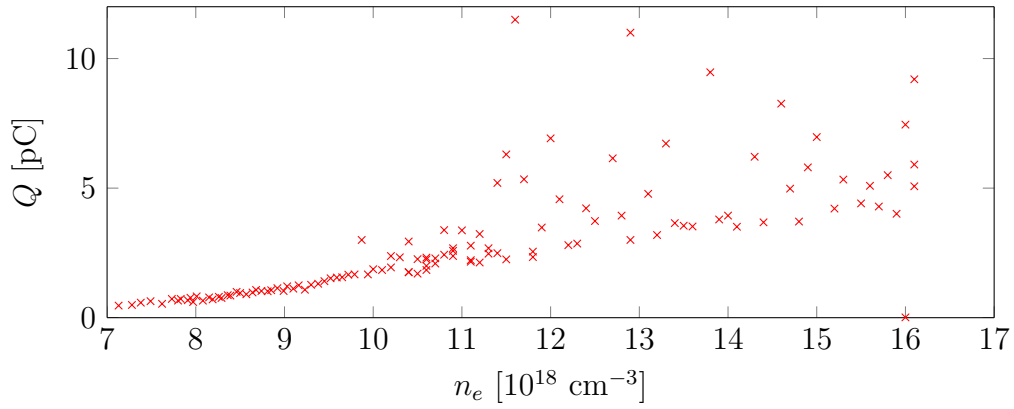

Figure 5.5: Injected charge as a function of peak density from experimental studies in Lund. [7]

amount of injected charge starts to fluctuate [7].

In order to explain this, three simulations were conducted, by Xavier Davoine, with different densities, going as high as $15 \cdot 10^{18}$ cm^{-3}, but the discontinuity of the injected charge plot were not seen. These simulations served as a starting point for this part of the thesis.

The scanned simulation profiles are described in Figure (5.6). Note that in these simulations, both the temporal profile and a_0 was varied, but the total energy of the laser pulse was kept constant.

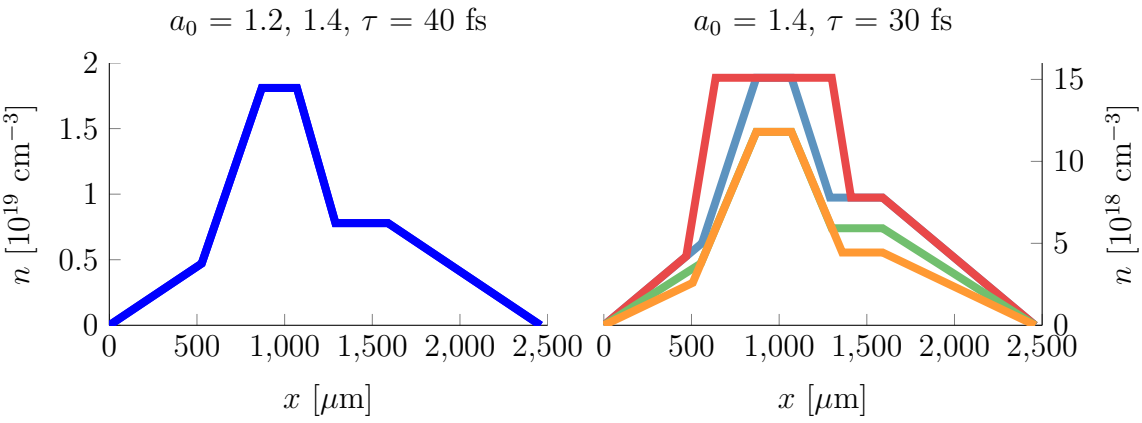

Figure 5.6: Density plots of the simulations. To the left a density profile simulated with two different laser parameters. To the right 4 different density profiles simulated with the same laser parameters.

First, the peak density was increased from $15 \cdot 10^{18}$ cm^{-3} to $18 \cdot 10^{18}$ cm^{-3} see if self-injection occurred, however, to see self-injection, the simulation had to go too far from the experimental data.

Instead, the laser parameters were modified, we decreased the pulse duration to 30 fs from 40 fs, and increased a_0 from 1.2 to 1.4, yielding better results. The simulations confirmed that for a peak density $11 \cdot 10^{18}$ cm^{-3} with $a_0 = 1.4$ and the temporal FWHM was 30 fs, self-injection did occur, thus breaking the nice control of injected charge at lower densities as seen in (See Figure (5.5)). In Figure (5.7) an energy spectrum from the simulations with a peak density of $12 \cdot 10^{18}$ cm^{-3} and a laser vector potential of 1.4 is presented. Three distinct charge peaks separated in energy are visible. The

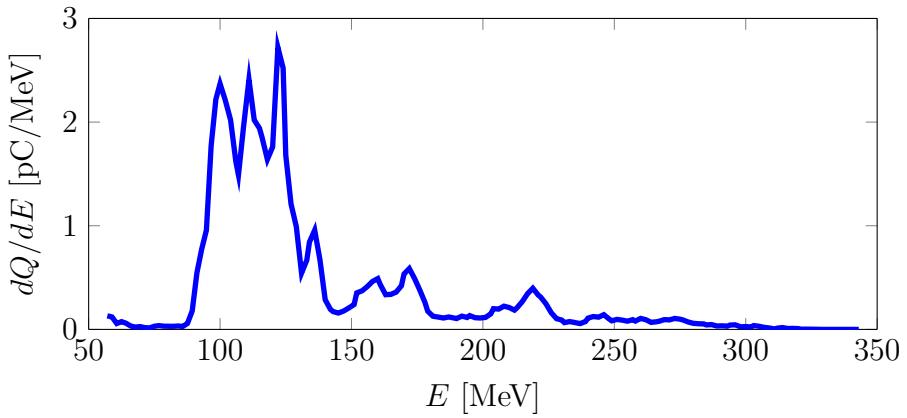

Figure 5.7: The energy distribution of a simulated experiment with a peak density $n_{peak} = 12 \cdot 10^{18}$ cm^{-3} and a laser vector potential of 1.4 is presented. One can see three distinct charge peaks in the spectrum, indicating that injection occurred at three different locations. The biggest one with the lowest energy (between 100 and 120 MeV) that was injected during the long down-ramp at the end of the density profile. With higher energy, there are two more peaks (around 160 and 220 MeV) from injection at two different, earlier locations. One bunch of electrons from self-injection at the upper plateau, and one bunch injected at the gradient.

first peak, lowest in energy between 100 and 120 MeV, the second around 160 Mev and the third around 220 MeV. These separated energy peak suggests there were three different injection mechanisms.

In a way this kind of simulations requires more work than the ones presented later. Partly because one has to simulate the full experiment and that requires more computing time. Partly because one also has to know in which measured quantity one has the highest uncertainty.

Note that these simulation, where a longer density profile designed to

imitate a real experiment, the energy spectrum in Figure (5.7) is not as clean as the simulations presented in the parametric scans later. This is due to the fact that the data is taken from vacuum after the electrons have left the plasma. On their way out electrons have then passed a down-ramp gradient, and therefore got more charge injected that does not have time to be accelerated to high energies.

Influence of density down-ramp length

For the parametric scans the laser parameters were kept constant at $a_0 = 1.8$. The FWHM pulse duration was kept at 30 fs, and the spot size of the beam was 18 µm. The beam focus plane was located in the beginning of the upper plateau. For these laser parameters it was observed in a first simulation that the laser pulse alone propagating in a constant density of $6 \cdot 10^{18}$ cm^{-3} did not trigger self-injection over distances of the upper plateau.

The moving window measured 51 µm along the optical axis and 65 µm in radial direction for most runs. The time step was kept at 52 attoseconds and the spatial grid measured 16 nm in x and 127 in r. Two azimuthal Fourier-modes were used throughout the simulations. In order to keep at least one full plasma wavelength within the moving window, the box size was increased for the runs containing densities below $n_e = 3 \cdot 10^8$ cm^{-3}.

To check that simulating only one period reproduced the physics properly, a reference run was performed with a twice as long simulation box, showing that the longitudinal phase-space (electron distribution as a function of the longitudinal momentum px and longitudinal position x) distribution of electrons are almost identical in the two cases. This data is presented in Figure (5.8).

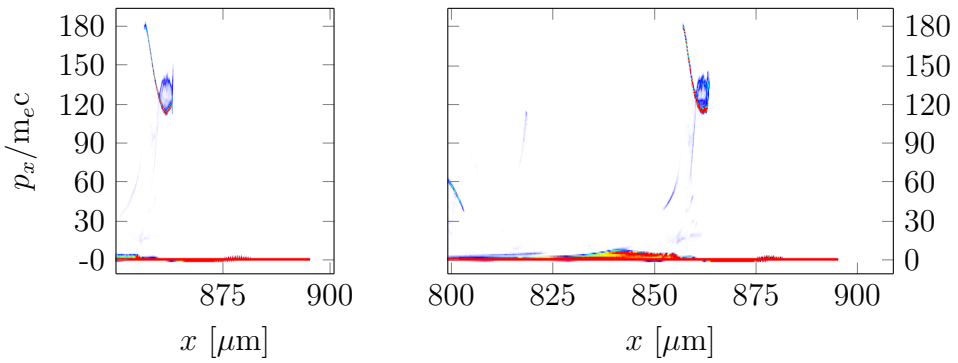

Figure 5.8: Comparison of phase-space distribution of electrons for two simulations with different size of the moving window.

A sequence of nine simulations were performed to study the influence of the length of the density down-ramp. This was done by varying n_{acc} while keeping $\Delta n/l$ constant. The density profiles of the simulations are described in Figure (5.9).

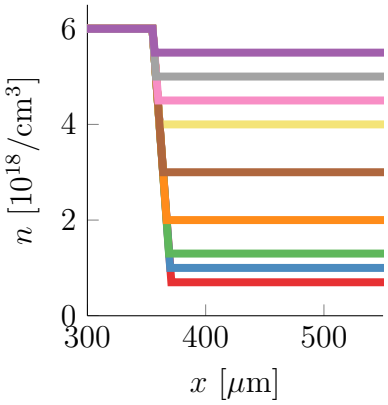

Figure 5.9: A description of the down-ramp density profiles. $\Delta n/l$ was kept constant by varying n_acc and l simultaneously to increase the length but not the slope of the gradient. The laser's beam waist was placed at the start of the peak density. The total simulation length is 900 µm. a sharp up-ramp gradient starts the density profile, and a similar down-ramp gradient ends it.

In the phase-space distribution of electrons, there is a clear separation in momentum between the background electrons and the injected electrons- From the phase-space distribution, the total number of injected electrons are integrated. This was done for each case, the results can be seen in Figure (5.10).

A linear trend between the lower plateau density n_{acc} and the amount of injected charge at the gradient could be seen for density differences on the order of $\Delta n = 0.5 - 5.5 \cdot 10^{18}\text{cm}^{-3}$. However, for density differences below $\Delta n = 1.5 \cdot 10^{18}$ cm^{-3} injection occurred both in the density down-ramp and again in the lower plateau resulting in a different total charge (shown as red dots in the diagram).

Over the density ranges in Figure (5.9), the formation of a plasma bubble varies a lot. This can be seen in Figure (5.11). In the figure, the left density cross section plot a bubble can still be easily defined, in this case, the prime driver of the wakefield is the laser. In the latter, the bubble is no longer closed, and it seems like the electron bunch itself is driving part of the wakefield.

Lu et al. have theoretically mapped the bubble regime and set up criteria for the amount of power a laser pulse need to drive a wake into the bubble regime [23]. Calculations based on this article shows that the so-called critical

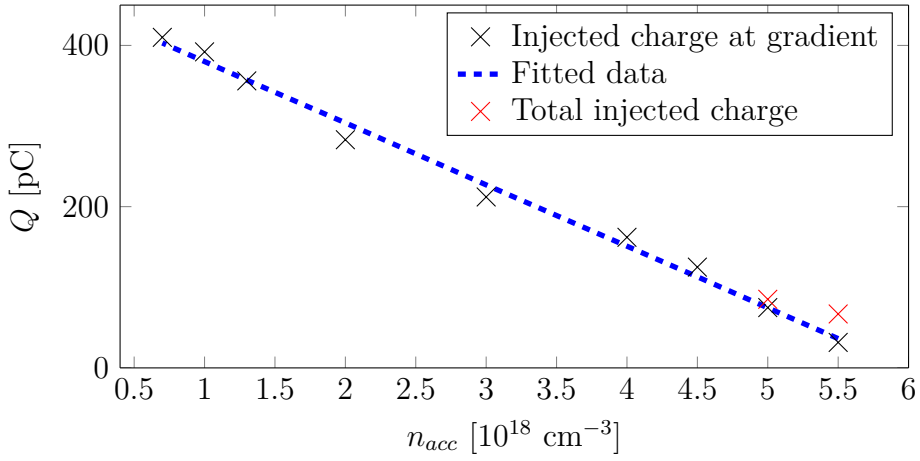

Figure 5.10: Injected charge as a function of the lower plateau's density.

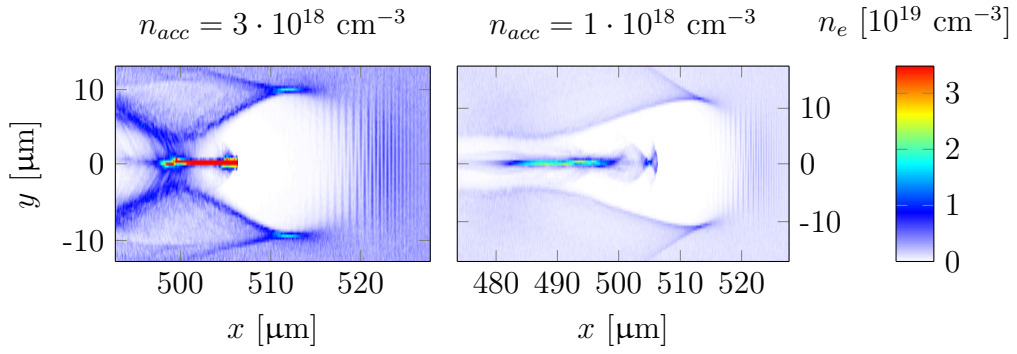

Figure 5.11: Post gradient acceleration in $n_e = 3 \cdot 10^{18}$ and $n_e = 1 \cdot 10^{18}$. Note how one can still define a "bubble" to the left and that the longitudinal spatial injected charge distribution is smaller.

power for for a laser pulse, is not reached with the energy left after the gradient for densities below $1 \cdot 10^{18}$e/cm^3. So the rather different shape of the bubble at the lower densities is probably an effect from a bad matching between laser power and density.

Even though the behaviour in the acceleration length seems very different (Figure (5.11)), the injected charge seems to scale linearly with the density difference which indicates that this does not affect the injection mechanism.

The energy distribution of the injected electrons in the different simulations after the same acceleration length can be seen in Figure (5.12). The energy of the peak in the distribution decreases with a lower density in the acceleration region as expected.

It is clear from Figure (5.12) that the strength of the wakefield decreases

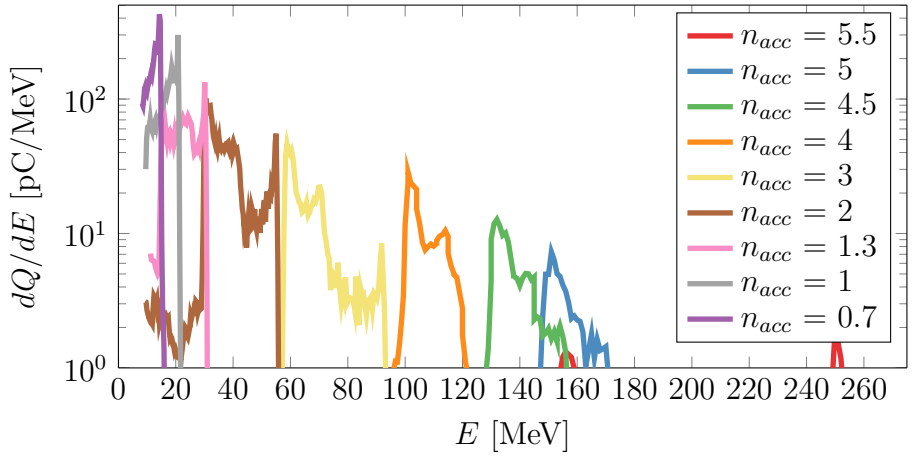

Figure 5.12: The energy distribution of electrons after an accelerating length of approximately 500 µm after the gradient.

with n_{acc} since the energy of the electrons are lower. The electric field perceived by an electron is influenced by two effects: The position within the plasma density wave, the wakefield amplitude depends on the position within the wave, and the overall strength of the wakefield, which scales with the plasma density. Furthermore, one can draw the conclusion that the cases where $n_{acc} < 3 \cdot 10^{18}$ cm^{-3} would not be useful for wakefield acceleration. This is due to the fact that the accelerating region has a very low electron number density, and thus a low accelerating force for the injected electrons, and the amount of injected charge distorts the wakefield which makes the accelerating effect even weaker.

However, something interesting happens here for the highest value of n_{acc}, it seems to have two quasi mono-energetic charge peaks around 160 and 250 MeV in the energy distribution diagram. As mentioned earlier, for the runs where $\Delta n < 1.5 \cdot 10^{18}$ cm^{-3} injection occurs at two locations. The charge injected at the gradient is accelerated for a longer time, and therefore gain more energy, which results in two different separated energy peaks in Figure (5.12).

In addition, as the bubble only expands a small amount, the injected charge is deposited in the strongest parts of the accelerating field (See Figure (2.2)). This explains why the energy of this electron bunch is significantly higher than the others. The longitudinal spread of the injected electrons is also smaller, which means the whole bunch of electrons will experience a similar electric field throughout the acceleration. In turn, this preserves the initial energy spread better. This suggest that a short gradient is preferable, but it might be hard to achieve this experimentally. However, it also suggests that

lower densities are beneficial as well to avoid the second injection mechanism.

An analysis of the longitudinal electric field shows that the charge injected in all the other cases strongly distorts the wakefield after the density down-ramp due to beam loading (see Figure (5.13)), resulting in a lower accelerating field.

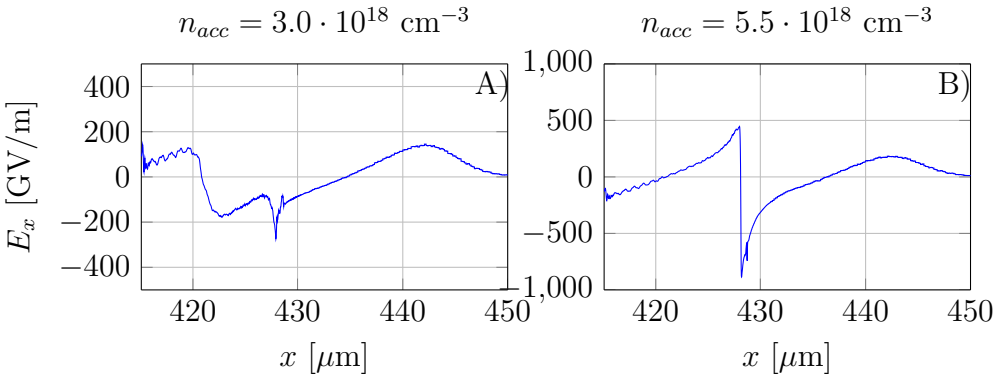

Figure 5.13: In A) the wakefield in is heavily influenced by the over 200 pC injected charge. The characteristic shape of the wakefield can no longer be seen. This is called beam loading. In B) the wakefield still has it characteristic shape, the 40 pC charge of electrons influence on the wake field is not that big.

The numerical results on the amount of injected charge dependence agrees well with an experiment conducted in Lund [7], described earlier in this thesis. It should be noted that in that experiment, the injected charge was much lower than shown in the simulations. Also the density down-ramp was longer, but a linear increase in charge could be seen when increasing n_{peak}.

Influence of the down-ramp slope

Another series of simulations were carried out in order to study the effect of the slope of the density down-ramp. In these simulations n_{acc} was kept constant while $\Delta n/l$ was varied. In Figure (5.14) a description of the density profiles simulated can be seen.

The amount of injected charge for the different cases was studied here as well and are shown in Figure (5.15). The relation between the density down-ramp slope and the amount of injected charge is not that easy to describe mathematically. We can clearly see a decrease in charge with an increasing slope length l. In the same figure a logarithmic version of the data is presented, where a straight line could be fitted to the data points.

In Figure (5.16) the energy distributions for the different density down-ramp slopes are presented. Here we see some interesting behaviour in the

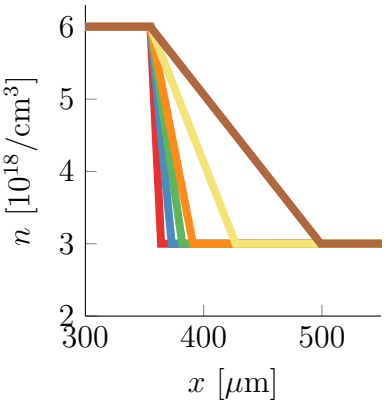

Figure 5.14: A background density description of the different runs while keeping the density ratio fixed while varying the gradient. The total simulation length is 900 µm, when a sharp upward gradient starts the density profile, and a similar downward gradient ends it.

energy distribution of the particles for the different simulations as well. It seems the gradient extending over almost 90 µm has the most peaked charge distribution.

The electron bunches get significantly higher energies in the simulations with longer slopes, this can be expected due to the following three contributing effects:

- The electrons are accelerated during the extent of the gradient, where they experience a higher background density for a longer time.
- The electrons will stay further back in the bubble a longer period of time, which means they experience a stronger electric field.
- There is less charge to accelerate, which means that the so-called beam loading effect is weaker, which in turn yields stronger accelerating fields.

In Figure (5.17) one can see that the deformation of the wakefield from the electrons is stronger in the steeper slope case.

The charge distribution in the injected bunches is presented in Figure (5.18). The spatial distribution of charge is over approximately the same length for all cases. This is due to the fact that the plasma wavelength increases the same amount over all slopes, in this parametric scan it is the expansion time we vary. The most peaked distribution in Figure (5.18) agrees with the most peaked spectrum in Figure (5.16). However, it is not clear that these two effects are connected. Furthermore, this indicates that the gradient can be tuned to get an optimal charge distribution within the bubble.

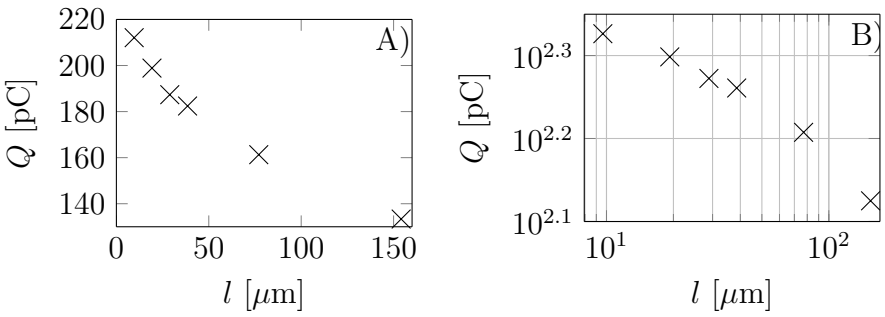

Figure 5.15: In A) the injected charge as a function the the density down-ramp slope length l is shown. The dependence is not linear. In B) the same data is plotted in a logarithmic diagram. Note how a straight line could be fitted to the data here.

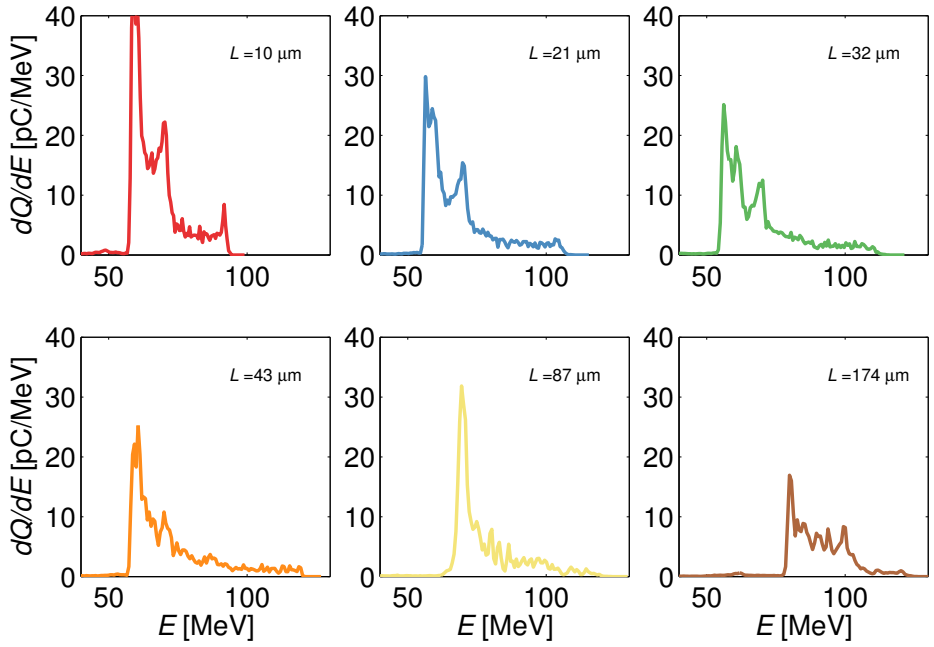

Figure 5.16: The energy distribution of electrons after an accelerating length of approximately 500 μm after the gradient when the length of the gradient was varied. n_{peak} was $6 \cdot 10^{18}$ cm^{-3} and n_{acc} was $3 \cdot 10^{18}$ cm^{-3}. Note the peaked energy spectrum for the run with a density down-ramp length $L = 87$ μm.

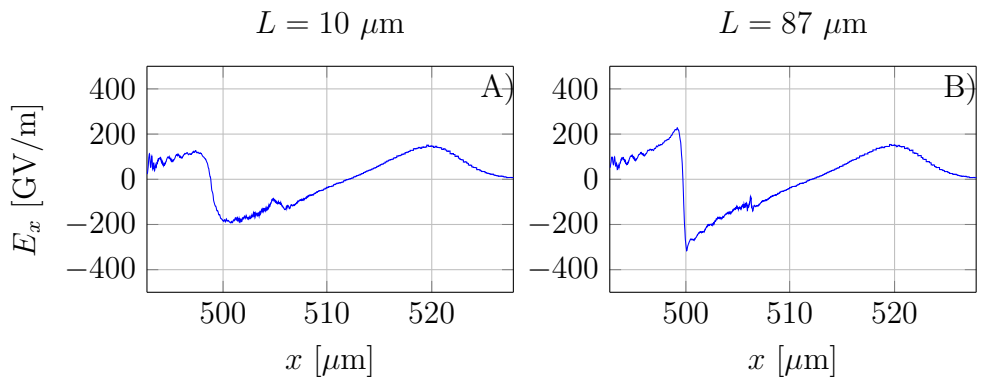

Figure 5.17: A) The wakefield is distorted, the typical nonlinear dip can not be seen. B) The wakefield is better preserved after injection than in A).

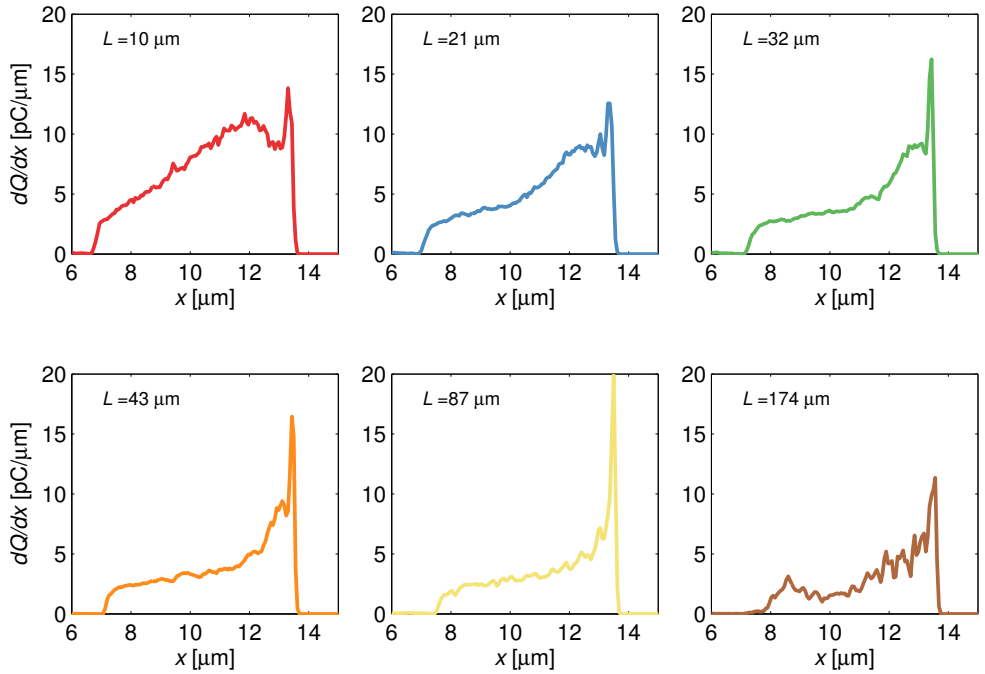

Figure 5.18: The spatial distribution of electrons along the optical axis as a function of length within the bubble after an accelerating length of approximately 500 µm after the gradient. Note the peaked distribution for the simulation with a density down-ramp length $L = 87$ µm.

Chapter 6

Conclusion and Outlook

The simulation of density down-ramp injection shows promising results. The amount of injected charge can be controlled by varying the density difference and down-ramp length. The gradient also plays a role in the injected charge, however, does not offer the same amount of control. To be able to realise the simulated density profiles experimentally will be a big challenge, it is not easy to create sharp reproducible density down-ramps. There is still a lot of work to be done in laser wakefield acceleration before it can be used as a stable electron source.

One thing that speaks in favor of density down-ramp injection is the stability shown in the experiment by Hansson et al. [7]. Injection occurred for every shot, and the standard deviation of injected charge was as low as 13 %, which in this field seems to be rare. For self-injection, the standard deviation of injected charge usually lies around 50 %. Perhaps a combination of ionisation and density modulation injection will be successful, as it yields more injected charge than pure gradient injection. One could imagine one region where the density is higher, where the laser is focused tighter and ionisation injection occurs, in combination with a lower density acceleration region, where the phase-space rotation and or dephasing criteria are met.

The top-view-setup needs a bit more work. Perhaps a camera with better dynamic range is needed to be able to see more of the plasma channel. The greatest benefit of top-view as an diagnostics is that it is easy to setup. If one could understand what causes the different phenomena that can be seen on the top-view images, it could be a fast and maybe reliable diagnostic to calibrate the experiment in the beginning. We can already see that functional wakefield accelerator leaves a thin, straight, relatively low-light trace in the beginning.

Whether it would work as a good diagnostic or not for gradient injection remains to be tested. Perhaps a gas jet target is more suitable for the top-view, as the gas cell puts an extra numerical aperture on the imaging system. There are several questions to be answered, some of which we might be able to answer from the simulations.

In conclusion, one of the main goals of this Master's project was to start running PIC-simulations both for independent studies of laser wakefield acceleration and to support the experiments on laser wakefield acceleration carried out in Lund and has been successfully completed. PIC-simulations are an essential tool for understanding the physical process of laser wakefield acceleration. Being able to simulate this in-house with an effective code such as CALDER-CIRC will improve the rate at which the group can do research.

References

[1] W. Leemans, A. Gonsalves, H.-S. Mao, K. Nakamura, C. Benedetti, C. Schroeder, C. Tóth, J. Daniels, D. Mittelberger, S. Bulanov, *et al.*, "Multi-GeV electron beams from capillary-discharge-guided subpetawatt laser pulses in the self-trapping regime," *Physical Review Letters*, vol. 113, no. 24, p. 245002, 2014.

[2] T. Tajima and J. Dawson, "Laser electron accelerator," *Physical Review Letters*, vol. 43, no. 4, p. 267, 1979.

[3] J. Faure, Y. Glinec, A. Pukhov, S. Kiselev, S. Gordienko, E. Lefebvre, J.-P. Rousseau, F. Burgy, and V. Malka, "A laser–plasma accelerator producing monoenergetic electron beams," *Nature*, vol. 431, no. 7008, pp. 541–544, 2004.

[4] S. Mangles, C. Murphy, Z. Najmudin, A. Thomas, J. Collier, A. Dangor, E. Divall, P. Foster, J. Gallacher, C. Hooker, *et al.*, "Monoenergetic beams of relativistic electrons from intense laser–plasma interactions," *Nature*, vol. 431, no. 7008, pp. 535–538, 2004.

[5] C. Geddes, C. Toth, J. Van Tilborg, E. Esarey, C. Schroeder, D. Bruhwiler, C. Nieter, J. Cary, and W. Leemans, "High-quality electron beams from a laser wakefield accelerator using plasma-channel guiding," *Nature*, vol. 431, no. 7008, pp. 538–541, 2004.

[6] M. Burza, A. Gonoskov, K. Svensson, F. Wojda, A. Persson, M. Hansson, G. Genoud, M. Marklund, C.-G. Wahlström, and O. Lundh, "Laser wakefield acceleration using wire produced double density ramps," *Physical Review Special Topics-Accelerators and Beams*, vol. 16, no. 1, p. 011301, 2013.

[7] M. Hansson, B. Aurand, X. Davoine, H. Ekerfelt, K. Svensson, A. Persson, C. Wahlström, and O. Lundh, "Down-ramp injection and independently controlled acceleration of electrons in a tailored laser wakefield accelerator," *submitted*, 2015.

[8] F. F. Chen, *Introduction to plasma physics*. 227 West 17th Street, New York, N.Y. 10011: Plenum Press, 1976. Second printing.

[9] D. Umstadter, J. Kim, and E. Dodd, "Laser injection of ultrashort electron pulses into wakefield plasma waves," *Physical Review Letters*, vol. 76, no. 12, p. 2073, 1996.

[10] E. Esarey, R. Hubbard, W. Leemans, A. Ting, and P. Sprangle, "Electron injection into plasma wakefields by colliding laser pulses," *Physical Review Letters*, vol. 79, no. 14, p. 2682, 1997.

[11] J. Faure, C. Rechatin, A. Norlin, A. Lifschitz, Y. Glinec, and V. Malka, "Controlled injection and acceleration of electrons in plasma wakefields by colliding laser pulses," *Nature*, vol. 444, no. 7120, pp. 737–739, 2006.

[12] A. Pak, K. Marsh, S. Martins, W. Lu, W. Mori, and C. Joshi, "Injection and trapping of tunnel-ionized electrons into laser-produced wakes," *Physical Review Letters*, vol. 104, no. 2, p. 025003, 2010.

[13] C. McGuffey, A. Thomas, W. Schumaker, T. Matsuoka, V. Chvykov, F. Dollar, G. Kalintchenko, V. Yanovsky, A. Maksimchuk, K. Krushelnick, *et al.*, "Ionization induced trapping in a laser wakefield accelerator," *Physical Review Letters*, vol. 104, no. 2, p. 025004, 2010.

[14] M. Chen, E. Esarey, C. Schroeder, C. Geddes, and W. Leemans, "Theory of ionization-induced trapping in laser-plasma accelerators," *Physics of Plasmas*, vol. 19, no. 3, p. 033101, 2012.

[15] F. Desforges, B. Paradkar, M. Hansson, J. Ju, L. Senje, T. Audet, A. Persson, S. Dobosz-Dufrénoy, O. Lundh, G. Maynard, *et al.*, "Dynamics of ionization-induced electron injection in the high density regime of laser wakefield acceleration," *Physics of Plasmas*, vol. 21, no. 12, p. 120703, 2014.

[16] G. Golovin, S. Chen, N. Powers, C. Liu, S. Banerjee, J. Zhang, M. Zeng, Z. Sheng, and D. Umstadter, "Tunable monoenergetic electron beams from independently controllable laser-wakefield acceleration and injection," *Physical Review Special Topics-Accelerators and Beams*, vol. 18, no. 1, p. 011301, 2015.

[17] S. Bulanov, N. Naumova, F. Pegoraro, and J. Sakai, "Particle injection into the wave acceleration phase due to nonlinear wake wave breaking," *Physical Review E*, vol. 58, no. 5, p. R5257, 1998.

[18] J. Faure, C. Rechatin, O. Lundh, L. Ammoura, and V. Malka, "Injection and acceleration of quasimonoenergetic relativistic electron beams using

density gradients at the edges of a plasma channel," *Physics of Plasmas*, vol. 17, no. 8, p. 083107, 2010.

[19] C. K. Birdsall, "Particle-in-cell charged-particle simulations, plus Monte Carlo collisions with neutral atoms, PIC-MCC," *Plasma Science, IEEE Transactions on*, vol. 19, no. 2, pp. 65–85, 1991.

[20] A. Lifschitz, X. Davoine, E. Lefebvre, J. Faure, C. Rechatin, and V. Malka, "Particle-in-cell modelling of laser–plasma interaction using Fourier decomposition," *Journal of Computational Physics*, vol. 228, no. 5, pp. 1803–1814, 2009.

[21] J. D. Jackson, *Classical electrodynamics.* New York : Wiley, cop. 1962, 1962.

[22] P. Gibbon, P. Monot, T. Auguste, and G. Mainfray, "Measurable signatures of relativistic self-focusing in underdense plasmas," *Physics of Plasmas*, vol. 2, no. 4, pp. 1305–1310, 1995.

[23] W. Lu, M. Tzoufras, C. Joshi, F. Tsung, W. Mori, J. Vieira, R. Fonseca, and L. Silva, "Generating multi-GeV electron bunches using single stage laser wakefield acceleration in a 3D nonlinear regime," *Physical Review Special Topics-Accelerators and Beams*, vol. 10, no. 6, p. 061301, 2007.

[24] G. Cheriaux, B. Walker, L. Dimauro, P. Rousseau, F. Salin, and J. Chambaret, "Aberration-free stretcher design for ultrashort-pulse amplification," *Optics Letters*, vol. 21, no. 6, pp. 414–416, 1996.

Appendix A

Multi-Terawatt Laser system at Lund Laser Centre

An overview of the laser system can be seen in Figure (4.1). The oscillator Ti:Al_2O_3 crystal is pumped with 532 nm green light. A Kerr-effect mode locking cavity is used to create an 80 MHz pulse train with nJ pulses each with a pulse duration of 20-30 fs. Here the pulses have a bandwidth of around 50 nm. Prisms are used in the cavity to keep the different wavelengths travel the same distance, thus keeping the pulses compressed.

After the oscillator a Pockels cell and polarisers, that chooses 10 pulses per seconds to transmit to a pre-amplification stage before the pulses are stretched. Entering the pre-amplifier the pulses have been stretched due to dispersion in different components and no measures are taken to prevent this. In the pre-amplifier, the pulses are amplified from nJ energies to μJ.

The pulses then enter the stretcher, more specifically an Öffner Triplet grating pulse stretcher. Here, each pulse passes two times, losing 70 % of its incoming energy and stretches to roughly 350 ps which corresponds to a length of approximately 10 cm. The pulse is stretched by letting the different wavelength components experience different optical pathways, thus chirping the pulse. By stretching the pulses the intensity is kept at acceptable levels throughout the laser system. This is done in order to avoid second order contributions to the refractive index in the gain medium when the intensity increases and to avoid damages on the optics.

After being stretched, the pulses enter a regenerative amplifier. This is a stable laser cavity, where the in and out coupling is controlled by a Q-switch. Each pulse reaches an energy of 5 mJ after approximately 11 passes. The diameter of the beam is just above one millimeter. Note that from the oscillator, the pulse has already been amplified by a factor of a million.

A multi-pass amplifier is next in line. The pulses passes through a Ti:Al_2O_3 crystal that measures 15 mm in length and 18 mm diameter. The crystal is pumped with two frequency doubled Nd:YAG lasers, each producing a pumping beam of approximately 1 J per pulse. The beam is telescoped to a

diameter of 9 mm. Leaving this region, the pulse has reached an energy of 350 mJ.

The pulses are split into two arms, where one of the beams with 220 mJ of energy is used for another experiment, and the pulse energy that is further amplified is approximately 100 mJ. The pulses are focused with a lens and sent through a spatial filter with a diameter of 0.5 mm to clean the spatial profile before entering the last amplification table.

The final amplifying crystal is pumped with five Nd:YAG lasers producing a total pump energy of 8 J per pulse. The crystal measures 25 x 25 x 20 mm and here each pulse is amplified to an energy of up to 2 J. A butterfly setup is used here as well. Before leaving the table, the pulse is telescoped to a diameter of 4 cm.

The pulse is then compressed to a pulse duration down to 30 fs. This is done using two gratings, letting the different wavelength components gather again by inverting the stretching mechanism in the Öffner triplet stretcher [24]. Before sending the pulse to the target, a deformable mirror is used to adjust the wavefront.

The throughput to target is 65%. Here the peak power reaches 40 TW. The compressor, and everything after, has to be in vacuum since the the pulse would ionise and interact strongly with air.

Appendix B

CALDER-CIRC input file

A typical CALDER-CIRC input file, together with comments in English, is presented here. Note that the original language is French, which is why the block headers (e.g. prot_reprise) are french abbreviations. It can also be useful to note that CALCER-CIRC originates from the code CALDER, which is why some of the parameters for different coordinates are not used.

Between every instruction block there should be one and only one line. A block begins with a keyword, where the first 8 letters are read, anything after those letter on the same line will be ignored. The line following the head line for each block is a description line, usually describing the parameters to be entered below. After this there will be a line, or a few lines, with parameters. These description and parameter lines can then be repeated, depending on the block used. An example block:

```
ordre_interp                I can write anything I want here
*** Order of interpolation ---- This is a description line
% This line should be removed in the input file.
3                             This is a parameter line
This line should be blank
```

An example input file, please note that lines beginning with % has to be removed for the actual input file. Everything on one line after % can be removed and fills no function.

```
******** Data file for K_lder ----------------------------------------------------
********-------------------------------------------------------------------------
prot_reprise %restart option, save the full state of the simulation
******** restart (0/1), protection (0/1), periodicity of protection --------------
0   0     2600

ordre_interp %interpolation order
******** ordre du facteur de forme -----------------------------------------------
3

partition %Keep dividable by the number of cores on your nodes
******** Number of cores per direction x, r, rest(keep as 1) ----------------------
100  4   1

cond_limites % Boundary Condition: -1 periodic, -2 absorbing, -3 reflecting
******** Particle BC:s -/+x, -/+r, -/+rest ----------------------------------------
-2  -2  -2  -2  -3  -3
```

```
******** Field BC:s -/+x, -/+r, -/+rest ----------------------------------------
-2  -2  -3  -3  -1  -1

maillage_spatial %Computational grid in normalised units
******** cell size x, r, rest (c/w0) -------------------------------------------
0.125  1.5    1.
******** Total nbr of cells in x, r, nbr of fourier modes ----------------------
3200  400  1

nb_profils
******** Number of blocks to describe the plasma (taille_plasma) -----------------
2

taille_plasma %Describe the shape of the plasma
******** center position in x, r, rest, max_value --------------------------------
% max_value is in comparison to other descriptions,
% note that 1 corresponds to the defined density in esp_particule)
9660.   0.    0.   1.
******** width and ramps in x, y, z (one line for each) -------------------------
'trapz'     5655.   6830.     6830.    0.    0.
'trapz'     1000.      0.        0.    0.    0.
'trapz'     1000.      0.        0.    0.    0.
% Here you can describe different shapes, described in the manual.

taille_plasma
******** center position -------------------------------------------------------
7618.   0.    0.   3.333
******** width and ramps in x, y, z -------------------------------------------
'trapz'     1570.   2468.     2468.    0.    0.
'trapz'     1000.      0.        0.    0.    0.
'trapz'     1000.      0.        0.    0.    0.

temps_simule %Simulation time mesh dt < 1/sqrt(1/dx^2 + m^2/dr^2)
******** Time step, Nbr of steps -----------------------------------------------
0.122   170000

fen_glissante %Moving-Window
******** on/off, start movement time, finish, normalised speed ------------------
1   400  1e8   1.

src_laser %laser source,the first value is multiplied by 2*pi by the parser.
******** lambda, e_0, angle_y, angle_z, polar, chirp -----------------------------
% angle_y, angle_z are not used, keep them as 0
1.    1.2    0.   0.   1.   0.0
******** time profile: type, order, length, keep 0 with gauss, max ---------------
'gauss'                  1       94.2       0.0   180.
******** radial profile r : type, order, width (FWHM intensity), ramp, center ----
'focrz'                  1      150.     1800.      0.
******** rest-profile: For CALDER-CIRC, keep same as radial profile --------------
'focrz'                  1      150.     1800.      0.
% These shapes are described in the manual of CALDER

especes_plasma  %Plasma species
******** fluid species, particle species, max nbr of particles per core ----------
% Fluid species is not implemented for CALDER-CIRC, always use 0
0   1   5000000

esp_particule %plasma (electron) species specification
******** creation, nbr per cell, dynamics, radiative loss, time steps EoM--
% For dynamics 1 means classical, 2 means relativistic
% Keep radiative loss as 0
% The last one is the is the rep rate at which the equation of motion is solved.
```

```
1  45  2  0  1
********Time steps between sorting particles in memory --------------------------
% This is not implemented in CALDER-CIRC, keep higher than number of time steps
15000000
******** Z nbr, Charge, mass, particle density ----------------------------------
-1  -1  1  0.00172
******** temperatures for x, y, z (keV), order of temperature -------------------
0.00  000.00  000.00   2
******** limits left and right for different species (c/w0) ---------------------
0.   900001

diag_type %Only text is working .vtk and paraview
******** ecr, txt, bin, hdf (hdf non implem., defaut=txt) ----------------------
'txt'

diag_temporels %diagnostic during the simulation
******** Ex^2, Er^2, Etheta^2, Bx^2, Br^2, Btheta^2 -----------------------------
1   1   1   1   1   1

champ_max (max fields)
******** nombre (nbr of fields that you will follow) ----------------------------
2
******** type et positions (which fields to plot)-------------------------------
'ex'
'er'

nb_diag_differents (facultatif, defauts = 4) %nbr of different diagnostics
******** nombre max. de diags spatiaux(space) et esp. phase ----------------------
4   3

diag_moyens % diagnostic average/mean
******** duree pour moyenne diags spatiaux et phases 1d --------------------------
6.283 0.

diag_phase space
******** Distribution function of specified parameters ---------------------------
2500   timesteps between dumps
-1   1     charge of particles included
'qx'         0.        0.      1600
%min, max (0. 0. means all particles will be included), nbr of points on histogram
'qy'         0.        0.       800
'qz'        -30.        30.       3
% dumping a large 3D-matrix will consume a lot of writing time for the first core
% and it will consume a lot of HDD space.

diag_phase
******** projection de l'espace des phases ---------------------------------------
2500
-1   1
'qx'         0.        0.       800
'px'         0.        0.       200
'00'         0.        0.         1

diag_spatial
******** field, average, periodicity of dump, min, max, periodicity --------------
'ex'     0      2500  0  0  1
% On average: 0 means off, 1 integral of the fields, 2 square of the integral
% Only 0 works if you use the moving window feature
% Choose a special data dump frequency for a defined period (last 3 values)
% 0 0 1 means off
    0.  1000000. 3200 % xmin xmax nbr of points
    0.      600.  400 % rmin rmax
```

```
    0.        0.    4 % Not used

dist_plasma
******** flag, type (1-2), periodicite -----------------------------------------
1    1   2500  (on/off, later, dump frequency)
******** center and width in x, y, z -------------------------------------------
  0.    900000.
  0.      500.   % Note that this is in x,y,z not x,r,theta
  0.      500.
******** energies max. (keV) des differentes especes ----------------------------
200.e3
%200 points in energy, 90 in theta, and 4 in phi, one energy for each species.

aide_debugging
******** verifications et messages pour la mise au point ---
3

fin_fichier %End of file
```

Appendix C

CALDER-CIRC outputs

In the input file (see Appendix B) you can specify diagnostic blocks, for example diag_spatial. This is how we get data to understand what happens in the simulation. All values given here are in normalised units.

C.1 Diag spat

The header of a typical output file from diag_spat (Field diagnostics) will look like

```
CHAMP er
3.050E+02 0
  0  3200   801  0.000E+00
  0   400   401  0.000E+00
  0     1     2  0.000E+00
[...]
```

The first line tells us what direction we are looking at. (Champ means field, er is says it is in the radial direction) The second line informs us of the time in the simulation the data was written (the zero after is irrelevant). The following three lines contains information about our three dimensions (being x,r and m). The first two value tells us between which cells we dump information (as specified in the input file). The third value reveals how many data points are actually written (On the third line we dump every fourth value in this direction). The last value corresponds to the zeroth's cells position. In this example, the moving window didn't start to move as of yet, which is why it is 0.

The fifth line is special since it corresponds to the number of modes m rather than a dimension we are used to. How to get the field from these is explained in Section 3.2.

After this follows a 801 * 2 x 401 x 2 dimensioned matrix, where the extra 2 comes from the values being complex. The first number is the real part, the second number is the imaginary part, then the value for the next cell follows.

C.2 Diag phase

The header of a typical output file from diag_pha (Particle diagnostic) will look like

```
PHASE_2D
qx
px
  3.05000E+02
    1
 -1.00000E+00  1.00000E+00
  0.000E+00  4.000E+02  800
 -8.363E-02  7.285E-01  200
  [...]
```

The first line tells us this is a 2D diagnostic. The second and third lines informs us what dimensions we map. The fourth line is the time of the dump. For the 2D version we ignore line five and six. On line seven and eight we get the minimum-, maximum-value and the number of data points for the repsective dimension mentioned on line two and three. After this a 800 x 200 matrix follows.

For the 3D case of diag_pha we have

```
PHASE_3D
qx
qy
qz
  3.05000E+02
    1
 -1.00000E+00  1.00000E+00
  0.000E+00  4.000E+02  800
 -6.000E+02  6.000E+02  400
 -3.000E+01  3.000E+01    3
 [...]
```

which is the same as above, except there is now an extra line describing the third dimension, and the matrix below is 800 x 400 x 3.

Appendix D

Populärvetenskaplig artikel

Acceleration av elektroner bakom en laserpuls

Partikelacceleratorer blir bara större och större. Man har nått en gräns för hur starka elektriska fält som kan skapas i de klassiska konstruktionerna. När fälten blir för starka kommer materialet de är gjorda av att joniseras och de accelererande fälten kommer att förstöras. Därför får man istället bygga längre och längre accelerationssträckor.

I en ny metod för elektronacceleration använder man istället plasma som medium för att accelerera partiklarna. Ett plasma består av redan joniserade atomer och icke-bundna elektroner. Plasmor är ovanliga på jorden, men är troligen den vanligaste formen av materia i universum. En stjärna är t.ex. en enda stor plasmaboll.

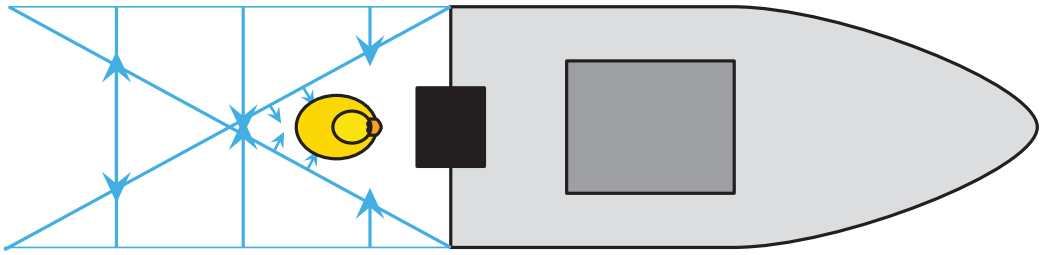

Figure D.1: Acceleration av en gummianka bakom en motorbåt. I kölvattnet efter till exempel en båt kan saker accelereras. Du kan själv prova genom att dra en slev framför en badanka i vatten hemma och se vad som händer.

Fördelen med ett plasma är att atomerna redan är nedbrutna, d.v.s. de kan inte slitas sönder av elektriska fält. Det kan därför existera mycket starkare elektriska fält i ett plasma än i t.ex. en metalltub, som används i konventionella acceleratorer. Genom att fokusera en laserpuls på ett plasma kan elektriska

fält skapas som är 10 000 gånger starkare än vad man kan nå i konventionella acceleratorer, vilket innebär att man kan förkorta accelerationssträckan lika mycket!

Processen kan liknas vid en motorbåt som åker på vatten (se Figur D.1). Där båten åker puttas vatten undan, och precis bakom bildas svallvågor på grund av att vattnet vill jämnas ut och återvänder dit båten har varit. Då bildas en störning som fortplantar sig i form av en svallvåg.

Hur fungerar då detta med laser och plasmor? Jo, man kan idag skapa väldigt starka laserpulser. Laserpulserna kan liknas vid en motorbåt som åker genom vatten. Istället för vatten puttas elektroner bort i plasmat medan joner blir kvar eftersom de är mycket tyngre och tidsskalan är mycket kort. Elektronerna kommer då känna en kraft från jonerna och dras tillbaka. De återvändande elektronerna kommer inte att hinna stanna i mitten, och detta leder till att det bildas en elektrondensitetsvåg i plasmat efter laserpulsen. I denna våg som bildas i svallet efter laserpulsen uppstår väldigt starka elektriska fält under korta tidsperioder. Dessa fält kan man använda för att accelerera ett fåtal elektroner. I Figur D.2 visas en schematisk bild över densitetsvågorna som bildas.

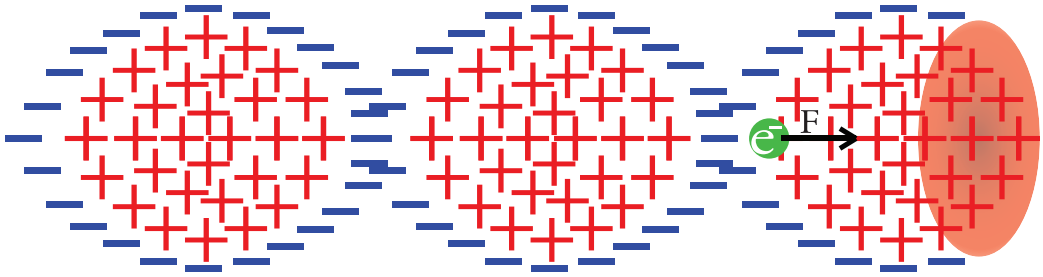

Figure D.2: Längst fram syns en laserpuls som plogar sin väg genom plasmat. Efter den bildas en densitetsvåg där elektroner och joner separeras. I de bubbelliknande strukturerna efter laserpulsen finns väldigt starka elektriska fält som kan användas för att accelerera elektroner. En grön testelektron har placerats i bakre delen av en bubbla, och kommer då att accelereras mot mitten på bubblan.

Hur lång tid det tar för elektronerna att återvända beror på bakgrundsdensiteten i plasmat. Ju fler joner det finns efter laserpulsen desto starkare kommer det elektriska fältet som drar i elektronerna att vara. Genom att variera bakgrundsdensiteten kan man styra hur långa vågorna ska vara efter laserpulsen.

Vad är då haken? Jo, för att kunna utnyttja dessa oerhört starka elektriska fält måste man fånga elektroner i bubblan precis bakom laserpulsen, där de kan puttas framåt av det starka elektriska fältet. Detta brukas kallas för

injektion av elektroner. Svårigheten ligger i att placera elektroner på ett kontrollerat sätt.

Jag har i mitt examensarbete använt mig av ett datorsimuleringsprogram för att numeriskt undersöka hur man skulle kunna kontrollera injektion av elektroner. Programmet är speciellt på så sätt att det inte körs på en persondator, utan har körts på 400 beräkningsenheter, så kallade kärnor, vilket ungefär motsvarar 100 vanliga datorer. Detta krävs för att simuleringarna är väldigt beräkningstunga.

I simuleringen skapar man partiklar som man puttar runt enligt Maxwells ekvationer, dvs de ekvationer som beskriver hur elektromagnetism beter sig. I ett typisk fall har jag simulerat över 60 miljoner partiklar som puttas omkring av en laserpuls i ungefär 60 tusen tidssteg.

Mer specifikt har jag studerat vad som händer om laserpulsen åker mellan två olika bakgrundsdensiteter av elektroner. Man kan då starta injektion genom att förlänga våglängden i densitetsvågen bakom laserpulsen. Detta har fördelen att om man kan kontrollera var man byter bakgrundsdensitet, kan man också kontrollera var injektion av elektroner sker.

Jag har bland annat studerat hur injicerade elektroner påverkas när man varierar skillnaden i bakgrundsdensitet och kommit fram till att det finns en linjär relation mellan injicerad laddning och densitetsskillnad. Jag har även tittat på vad som händer när man varierar hur snabbt man går från en densitet till en annan och ser där en minskande mängd injicerad laddning vid längre övergångar.

Sammanfattningsvis har jag numeriskt studerat och försökt karakterisera hur injektion av elektroner går till när man varierar bakgrundsdensiteten som laserpulsen propagerar igenom. Jag har identifierat trender i mängden injicerade elektroner då man varierar densitetsövergångarna på olika sätt.